Chemical Science

Cite this: *Chem. Sci.*, 2012, **3**, 1024

www.rsc.org/chemicalscience

EDGE ARTICLE

Direct observation of a ferri-to-ferromagnetic transition in a fluoride-bridged 3d–4f molecular cluster†

Jan Dreiser,*[a] Kasper S. Pedersen,*[b] Cinthia Piamonteze,[a] Stefano Rusponi,[c] Zaher Salman,[d] Md. Ehesan Ali,[e] Magnus Schau-Magnussen,[b] Christian Aa. Thuesen,[b] Stergios Piligkos,[b] Høgni Weihe,[b] Hannu Mutka,[f] Oliver Waldmann,[g] Peter Oppeneer,[h] Jesper Bendix,*[b] Frithjof Nolting[a] and Harald Brune[c]

Received 13th October 2011, Accepted 6th December 2011
DOI: 10.1039/c2sc00794k

We report on the synthesis, crystal structure and magnetic characterisation of the trinuclear, fluoride-bridged, molecular nanomagnet $[Dy(hfac)_3(H_2O)–CrF_2(py)_4–Dy(hfac)_3(NO_3)]$ (**1**) (hfacH = 1,1,1,5,5,5-hexafluoroacetylacetone, py = pyridine) and a closely related dinuclear species $[Dy(hfac)_4–CrF_2(py)_4]\cdot{}^1/_2\ CHCl_3$ (**2**). Element-specific magnetisation curves obtained on **1** by X-ray magnetic circular dichroism (XMCD) allow us to directly observe the field-induced transition from a *ferri*magnetic to a *ferro*magnetic arrangement of the Dy and Cr magnetic moments. By fitting a spin-Hamiltonian model to the XMCD data we extract a weak antiferromagnetic exchange coupling of $j = -0.18\ cm^{-1}$ between the Dy^{III} and Cr^{III} ions. The value found from XMCD is consistent with SQUID magnetometry and inelastic neutron scattering measurements. Furthermore, alternating current susceptibility and muon-spin relaxation measurements reveal that **1** shows thermally activated relaxation of magnetisation with a small effective barrier for magnetisation reversal of $\Delta_{eff} = 3\ cm^{-1}$. Density-functional theory calculations show that the Dy–Cr couplings originate from superexchange *via* the fluoride bridges.

Introduction

Lanthanides are promising building blocks for molecular magnetic materials: incorporating 4f ions in molecular clusters to form single-molecule magnets[1] (SMMs) is of high interest as 4f metals exhibit stronger spin–orbit coupling than their 3d counterparts and most of them possess a ground state characterised by an unquenched orbital momentum. The ligand-field splittings of the ground multiplet are typically on the order of the thermal energy at room temperature and result in large energy barriers for magnetisation reversal which are an important prerequisite to achieve long magnetisation-relaxation times.[2] This is especially well exemplified by mononuclear phtalocyaninate,[3] polyoxometalate,[4] organometallic[5] or purely inorganic[6] lanthanide compounds, all shown to exhibit SMM behaviour. Very recently, significant advances in the synthesis of polynuclear 4f clusters such as the achievements of record-high energy barriers up to ~530 K[7] and of a strong exchange coupling *via* a N_2^{3-} radical bridge[8] have been reported. Also, slow relaxation in some 3d–4f clusters[9] has recently been realised at temperatures comparable to those for 3d-only SMMs.

Understanding the magnetic behaviour of 4f-containing clusters is much more challenging than that of 3d-only systems. Determining the ligand-field parameters of 4f ions requires extensive studies, and the extraction of spin-Hamiltonian parameters such as intracluster magnetic exchange coupling can be tricky. In 3d clusters this information can in most cases be readily obtained from direct current (dc) magnetic susceptibility, while in the case of 4f it is often buried under the dominant effect of ligand-field splittings.[10] Not even the m_J of the ground-state can be taken for granted, as it depends on the exact ligand field.[11] To this end, X-ray magnetic circular dichroism[12,13] (XMCD) can provide clear-cut information and thus help in the

[a]*Swiss Light Source, Paul Scherrer Institut, CH-5232 Villigen PSI, Switzerland. E-mail: jan.dreiser@psi.ch*
[b]*Department of Chemistry, University of Copenhagen, DK-2100 Copenhagen, Denmark. E-mail: ksp@kiku.dk; bendix@kiku.dk*
[c]*Institute of Condensed Matter Physics, Ecole Polytechnique Fédérale de Lausanne, CH-1015 Lausanne, Switzerland*
[d]*Laboratory for Muon Spin Spectroscopy, Paul Scherrer Institut, CH-5232 Villigen PSI, Switzerland*
[e]*Center for Theoretical Chemistry, Ruhr-Universität Bochum, D-44801 Bochum, Germany*
[f]*Institut Laue-Langevin, F-38042 Grenoble Cedex 9, France*
[g]*Physikalisches Institut, Universität Freiburg, D-79104 Freiburg, Germany*
[h]*Department of Physics and Astronomy, Uppsala University, Box 516, S-751 20 Uppsala, Sweden*

† Electronic supplementary information (ESI) available: experimental section; thermal ellipsoid plots; XMCD sum rules analysis; details of ligand-field multiplet calculations; additional SQUID measurements on **1**; SQUID measurements on **2** and their analysis; analysis of the INS data and of the μSR measurements; details of the spin-Hamiltonian models; details of the DFT calculations. CCDC reference numbers 848193–848194. For ESI and crystallographic data in CIF or other electronic format see DOI: 10.1039/c2sc00794k

characterisation of 3d–4f compounds. Its main strength is the ability for measuring spin and orbital magnetic moments with elemental selectivity and ultrahigh sensitivity reaching down to submonolayers.

Here, we use XMCD to obtain element-specific magnetisation curves for the Dy^{III} and Cr^{III} ions in a novel type fluoride-bridged Dy^{III}–Cr^{III}–Dy^{III} cluster. Our data provide direct evidence for the field-induced transition from a ferrimagnetic to a ferromagnetic configuration of the magnetic moments in this trinuclear compound. This effect is manifested by a wiggle shape observed in the magnetisation curve of the Cr^{III} ion. Using spin-Hamiltonian models we are able to quantify the strength of the magnetic exchange coupling between Dy^{III} and Cr^{III} ions.

The vast majority of 4f[14] and mixed 3d–4f[9] clusters are bridged by oxide,[15] hydroxide[14a] or alkoxides.[2c,9] Here, we have been pursuing the possibilities of utilizing fluoride bridges—an approach which is nearly without precedence. This is intriguing as the fluoride ion proffers low basicity and a preference for pseudo-linear bridging, the latter facilitating prediction and design of specific molecular cluster topologies.[16] The synthesis of fluoride-bridged 3d–4f SMMs is obviously complicated due to the possible formation of insoluble lanthanide(III) fluoride. Nevertheless a few examples of fluoride-bridged 3d–4f clusters incorporating diamagnetic Ti^{IV} have been prepared by serendipitous approaches. The scarce examples include only $[La\{(C_5Me_4Et)_2Ti_2F_7\}_3]$ and $[Ln\{(C_5Me_5)_2Ti_2F_7\}_3]$ (Ln = Pr, Nd)[17,18] in which the 12-coordinate lanthanide ion is exclusively surrounded by fluoride ions. Recently the first clusters incorporating $\{Cr^{III}$–F–$Ln^{III}\}$ linking units were reported by Winpenny and co-workers.[19] The authors showed that reaction of a $\{Cr_6\}$ horseshoe $[(R_2NH_2)_3\{Cr_6F_{11}(O_2C^tBu)_{10}\}]_2$ (R = Et, ^{n}Pr) with dinuclear $[Ln(O_2C^tBu)_3(HO_2C^tBu)_3]_2$ yields mixed 3d–4f clusters with metal ion stoichiometries of $\{CeCr_6\}$, $\{Gd_2Cr_6\}$ and $\{Ln_4Cr_{12}\}$. However, in all of these, the $\{Cr^{III}$–F–$Ln^{III}\}$ units are further supported by carboxylate bridging. Some of us recently reported the first examples of Cr^{III}–Ln^{III} clusters containing unsupported {Cr–F–Ln} bridges.[20] The synthetic principle is based on the kinetic robustness of octahedral Cr^{III} complexes which suppresses the tendency of fluoride abstraction by the lanthanide ion.[21] Employment of another precursor; the *trans*-difluorido complex, *trans*-$[CrF_2(py)_4]NO_3$, has the advantage of being both robust and soluble in non-coordinating solvents such as chloroform.

In this work, we present a multi-technique study and the syntheses and structures of two fluoride-bridged Cr^{III}–Dy^{III} complexes: a trinuclear $[Dy(hfac)_3(H_2O)$–$CrF_2(py)_4$–$Dy(hfac)_3(NO_3)]$ (**1**) (hfacH = 1,1,1,5,5,5-hexafluoroacetyl-acetone, py = pyridine) and a dinuclear species $[Dy(hfac)_4$–$CrF_2(py)_4]\cdot{}^1/_2CHCl_3$ (**2**).

Results

Synthesis and structural analysis

Both **1** and **2** are obtained by the coordination of *trans*-$[CrF_2(py)_4]^+$ to $[Dy(hfac)_3(H_2O)_2]$ in chloroform solution. For the preparation of **1**, a large excess of $[Dy(hfac)_3(H_2O)_2]$ is needed to avoid precipitation of **2**. By using four equivalents of $[Dy(hfac)_3(H_2O)_2]$, pink needles of a trinuclear, fluoride-bridged asymmetric $[Dy(hfac)_3(H_2O)$–$CrF_2(py)_4$–$Dy(hfac)_3(NO_3)]$ cluster (**1**) result. The structures of **1** and **2** are depicted in Fig. 1, thermal-ellipsoid plots are shown in Figs. S1 and S2 (ESI†). **1** crystallises in the monoclinic space group *C*2/*c*. The coordination sphere of Dy(1) consists of three, bidentate $hfac^-$ ligands and one bidentate nitrate ion which is engaged in hydrogen bonding to a water molecule coordinated at Dy(3) in a neighbouring molecule. The central Cr^{III} ion is located on a crystallographic two-fold axis leading to systematic disorder of the water and nitrate coordinated to Dy. The Cr–F distance is 1.903(2) Å which is longer than the value found in the *trans*-$[CrF_2(py)_4]PF_6$ complex (Cr–F = 1.853(2) Å).[22] The pyridine ligands coordinated to Cr^{III} are arranged with a twist of approximately 30° following the twist of the $hfac^-$ ligands.

On the other hand, reaction of one-to-one stoichiometry yields red-violet, block-shaped crystals of $[Dy(hfac)_4$–$CrF_2(py)_4]\cdot{}^1/_2CHCl_3$ (**2**). **2** crystallises in the triclinic space group $P\bar{1}$ and contains an almost linear Cr–F–Dy bridge (177.74(7)°) between a $\{Cr^{III}F_2(py)_4\}^+$ and a $\{Dy(hfac)_4\}^-$ unit. The Cr^{III} ion is octahedrally coordinated whereas the 9-coordinate Dy^{III} can be described as tri-capped trigonal prismatic. The four bidentate $hfac^-$ ligands coordinated to Dy create a four-bladed propeller twist. The asymmetric unit contains both the Λ- and Δ-isomer of $[Dy(hfac)_4$–$CrF_2(py)_4]$. The Cr–F bond lengths of the bridging fluorides are significantly elongated (1.9145(14) Å and 1.9045(14) Å) compared to the non-bridging fluorides (1.8440(15) Å and 1.8416(15) Å). The Dy–F distances (2.3474(15) Å and 2.3245(14) Å) are shorter than the Dy–O bond lengths which are in the range 2.3689(18) Å to 2.4496(19) Å.

X-ray magnetic circular dichroism

Polarisation-dependent X-ray absorption spectra of **1** are shown in Fig. 2a and 3a. The spectra were taken at the Dy $M_{4,5}$ and the

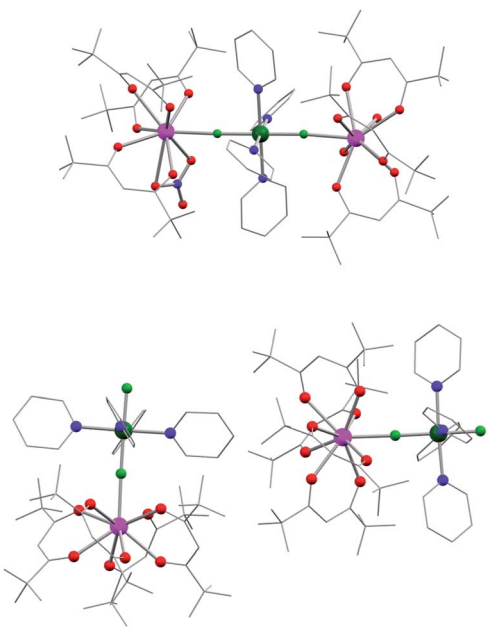

Fig. 1 Molecular structure of **1** (top) and **2** (bottom, both molecules in the asymmetric unit are shown) as obtained from X-ray diffraction. Color code: pink: Dy, dark green: Cr, light green: F, red: O, blue: N. Carbon skeletons and non-bridging fluorines are shown as wireframe and hydrogens and solvent molecule in **2** are omitted for clarity.

Cr $L_{2,3}$ edges at the indicated magnetic fields and temperatures. Clearly, the observed spectra of both Dy^{III} and Cr^{III} ions are strongly dichroic. Fig. 2c and 3c show the resulting XMCD spectra for the respective elements. While the XMCD of Dy is almost saturated at $B = 1$ T, this is not the case for Cr: here the XMCD signature flips its sign upon increasing the field from 1 T to 6 T corresponding to a field-induced flip of the Cr magnetic moment. This behaviour is also reflected in the element-specific magnetisation curves shown in Fig. 4a and 4b. Curve (a) is indicative for the Cr moment being antiparallel to the field at small, and parallel to it at large external field, while curve (b) indicates that the Dy moments behave similar to paramagnets with a saturation field around 2 T at 2 K. The data show some similarities to those recently observed on $TbPc_2$ molecules coupled to a ferromagnetic substrate.[13n] However, the curves on **1** are fully reversible without hysteresis. Black squares indicate the total (spin and orbital) Dy magnetic moments extracted from the XMCD spectra using sum rules[23] (for details see ESI†). Note that these moments represent the average over the two nonequivalent Dy sites in the trinuclear cluster because XMCD is element selective but not site selective.

The obtained ratio of $\langle L_z \rangle / \langle S_z \rangle$ is 1.9(4) for Dy, in excellent agreement with the value of 2.0 derived from Hund's rules. In the Cr case, the sum rules are not applicable because of the small energy separation between the Cr L_2 and L_3 edges.[24] Here, the absolute values of the Cr magnetic moments were extracted using ligand-field multiplet calculations (see ESI†).

SQUID magnetometry

Fig. 4c shows the cluster magnetisation curve of **1** obtained by SQUID magnetometry at 1.9 K. After a steep rise near zero field the slope reduces upon increasing the field but no clear saturation can be observed, suggesting strong anisotropy and/or the presence of low-energy excited states.

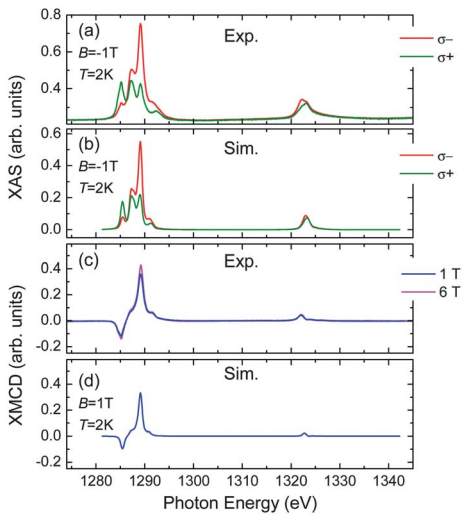

Fig. 2 (a) X-ray absorption spectra of **1** at the Dy $M_{4,5}$ edges recorded for two photon helicities at the indicated magnetic field and temperature. (b) X-ray absorption spectra obtained from ligand-field multiplet calculations. (c) XMCD spectra measured on **1** at different magnetic fields and $T = 2$ K. (d) Simulated XMCD spectrum. See ESI† for parameters of simulations (b) and (d).

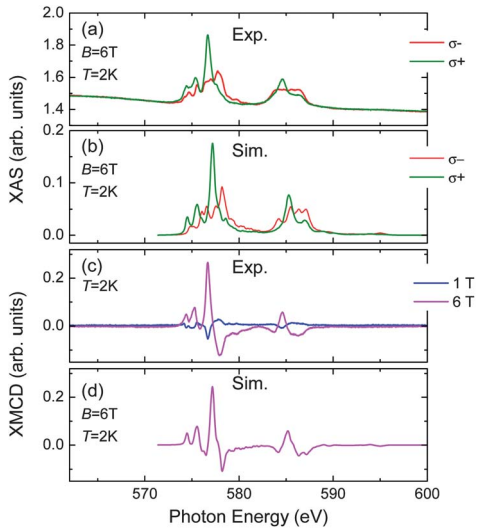

Fig. 3 (a) X-ray absorption spectra of **1** at the Cr $L_{2,3}$ edges recorded for two photon helicities at the indicated magnetic field and temperature. (b) X-ray absorption spectra obtained from ligand-field multiplet calculations. (c) XMCD spectra measured on **1** at different magnetic fields and $T = 2$ K. (d) Calculated XMCD spectrum. The simulation parameters for (b) and (d) are given in the ESI†.

Fig. 5 depicts the temperature dependence of the dc magnetic susceptibility of **1** represented as the χT product. When decreasing the temperature from 300 K, the susceptibility initially drops moderately. Upon further decrease the curve bends downwards and goes through a minimum at 4 K. In 3d-only transition-metal clusters with a magnetic ground state, this behaviour would indicate intramolecular antiferromagnetic interactions. However, this argument may fail for clusters containing 4f ions due to the orbital contribution to their magnetism.[10] The room-temperature value is $\chi T = 30.15$ cm^3 K mol^{-1} yielding perfect agreement with the value expected for two isolated Dy^{III} ions with $g_J = 4/3$ and a Cr^{III} ion with $g_S = 2$.

In the out-of-phase component of the ac susceptibility of **1**, a clearly frequency-dependent onset of a peak is observed within the accessible temperature ($T \geq 1.8$ K) and frequency (0.1–1500 Hz) range, as shown in Fig. 6a. This behaviour combined with

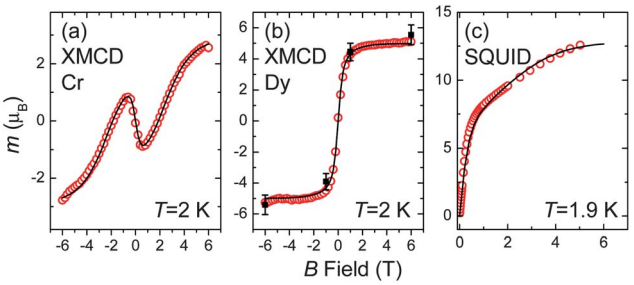

Fig. 4 Element-specific magnetisation curves of **1** for Cr (a) and Dy (b) measured at $T = 2$ K (red open circles). Black squares correspond to the total (spin and orbital) Dy magnetic moments obtained from sum rules at the respective fields. (c) Cluster magnetisation curve (red open circles) measured on **1** with SQUID magnetometry. Solid lines in (a,b,c) are the best-fit curves using Hamiltonian eqn (2).

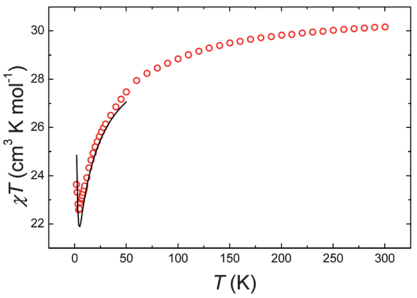

Fig. 5 Dc magnetic susceptibility of **1** (shown as the χT product, red open circles). The solid line shows the best fit using Hamiltonian eqn (1). We show this curve only up to 50 K, since the approximations of model eqn (1) do not hold beyond this temperature as discussed in the text.

the concomitant decrease in $\chi'(T)$ (see Fig. S4, ESI†) qualifies **1** as a SMM.

Muon-spin relaxation

To study the magnetisation dynamics of **1** at much shorter timescales than possible with our SQUID magnetometer we performed μSR experiments. The muons are used as local probes of magnetic fields originating from the different magnetic ions in the cluster. The μSR technique is sensitive to magnetic field fluctuations on timescales of $\sim 10^{-4}$–10^{-11} s, hence it covers a unique range of spin dynamics.[25] The temperature dependence of the magnetisation relaxation time displays Arrhenius behaviour as shown in Fig. 6b suggesting thermally-activated relaxation. From the fit a barrier of $\Delta_{\mathrm{eff}} = 3.0(2)$ cm^{-1} and a preexponential factor of $\tau_0 = 5.3(4) \times 10^{-8}$ s are obtained. The small effective barrier readily explains the absence of a hysteresis and why no maximum in the out-of-phase ac susceptibility was observed in the accessible frequency and temperature range.

Inelastic neutron scattering

Fig. 7a and 7b show the powder INS spectra obtained on **1** for the indicated wavelengths and temperatures. The data were summed over the |**Q**| range from 0.9 to 1.8 Å^{-1}. In the high-energy measurements shown in Fig. 7a, a single magnetic feature is detected (peak I). The higher-resolution spectra shown in Fig. 7b reveal a three-fold splitting of peak I. All sub-peaks are of magnetic origin and can be attributed to transitions in the level scheme indicated in the inset of Fig. 7b. Details are given in the ESI†.

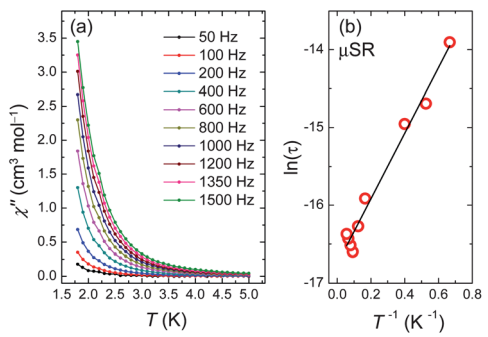

Fig. 6 (a) Out-of-phase component of the ac susceptibility (χ'') of **1** as a function of temperature at selected frequencies of the oscillating magnetic field obtained with $H_{\mathrm{dc}} = 50$ mT. (b) Arrhenius plot of the magnetisation relaxation time of **1** measured by μSR (red open circles) at zero magnetic field. The solid line is a fit to the Arrhenius law, yielding a barrier of $\Delta_{\mathrm{eff}} = 3.0(2)$ cm^{-1} and a prefactor of $\tau_0 = 5.3(4) \times 10^{-8}$ s.

Spin-Hamiltonian models

In order to extract quantitative information and to gain a deeper understanding of our data we have employed spin-Hamiltonian models. According to Hund's rules the ground state of the free Dy^{III} ion is $^6H_{15/2}$. As a consequence of spin–orbit coupling, the first excited multiplet $^6H_{13/2}$ lies about 4000 cm^{-1} higher in energy.[26] Furthermore, in the presence of a ligand field the ground multiplet splits into eight Kramers doublets over an energy scale of typically hundreds of wave numbers,[27] and depending on the exact nature of the ligand field different ground state doublets (*e.g.* ±15/2, ±13/2) have been reported.[11] The experimental determination of the ground-state doublet from powder magnetization and susceptibility measurements can be problematic in 4f-containing clusters, in particular, when the symmetry of the ligand field is low. It has been shown recently that *ab initio* calculations can give insight here.[28]

As a compromise between efficient calculations and reproduction of a maximum of the experimental data we use a Hamiltonian which operates in the restricted space of the ground state and the first-excited state Kramers doublets of each of the three ions. This *excited-state* (*encompassing*) *Hamiltonian* takes the form

$$\begin{aligned}\hat{H} = &-j_{12}\hat{\mathbf{J}}_1\cdot\hat{\mathbf{S}}_2 - j_{23}\hat{\mathbf{S}}_2\cdot\hat{\mathbf{J}}_3 - j_{13}\hat{\mathbf{J}}_1\cdot\hat{\mathbf{J}}_3 \\ &+\sum_i\left[D_i\left(\hat{S}_{i,z}^2 - \frac{1}{3}S_i(S_i+1)\right) + d_i\right] \\ &+\mu_B\sum_{i=1,3} g_i\hat{\mathbf{J}}_i\cdot\mathbf{B} + \mu_B g_2\hat{\mathbf{S}}_2\cdot\mathbf{B}.\end{aligned} \quad (1)$$

The first two terms represent isotropic nearest-neighbour exchange couplings, and the third term is a much weaker

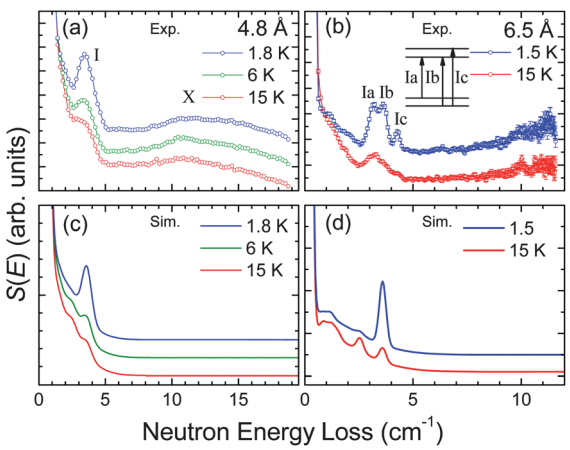

Fig. 7 (a, b) Inelastic neutron scattering spectra of **1** taken at the indicated wavelengths and temperatures. The intensity was summed over the useable |**Q**| range. The curves were offset to improve visibility. Error bars in (a) are smaller than the symbols. Inset in (b): level scheme obtained from the peak positions and the temperature dependence of the fine structure in (b). (c,d) Simulated INS spectra using eqn (1) with the best-fit parameters given in the text.

coupling between the Dy^{III} ions. At first sight the fourth anisotropy term describing the single-ion anisotropies seems unusual, but the proper choice of D_1, D_3, d_1 and d_3 simply generates splittings δ_1 and δ_3 between ground-state and first-excited-state doublets for the Dy^{III} ions.[29] In the fitting process it was found that the excited doublet of Dy(3) was not necessary to reproduce the experimental results; consequently it was neglected. For the Cr^{III} ion d_2 has to be zero. At low temperatures eqn (1) is an excellent approximation because of the large 4f-anisotropy splittings mentioned earlier. However, this approximation only holds as long as the population of energy levels higher than the first-excited doublet is negligible (see below). A similar model has been successfully applied in the case of a Dy_3 triangle.[30]

The model can be made more effective, when considering the ground-state Kramers doublets only. In this simplest and widely used[31] model the Dy^{III} ions are described by an effective angular momentum or pseudospin $S_1 = S_3 = 1/2$. The corresponding *spin-1/2* Hamiltonian reads

$$\hat{H} = -\sum_{i<k} \hat{\mathbf{S}}_i \cdot \mathbf{j}_{ik,\mathrm{eff}} \cdot \hat{\mathbf{S}}_k + D_2\left[\hat{S}_{2,z}^2 - \frac{1}{3}S_2(S_2+1)\right] + \mu_B \sum_i \hat{\mathbf{S}}_i \cdot \mathbf{g}_{i,\mathrm{eff}} \cdot \mathbf{B}. \quad (2)$$

Obviously, ligand-field (anisotropic) terms are meaningless for a spin-$^1/_2$ system, hence only the Cr anisotropy remains here. However, it is important to note that the anisotropy of the Dy^{III} ions is now contained in the $\mathbf{j}_{ik,\mathrm{eff}}$ and $\mathbf{g}_{i,\mathrm{eff}}$ matrices with diagonal entries $\{j_{ik,\mathrm{eff},xy}; j_{ik,\mathrm{eff},xy}; j_{ik,\mathrm{eff},z}\}$ and similar for $\mathbf{g}_{i,\mathrm{eff}}$. For simplicity, in both models, eqn (1) and (2), it was assumed that all main anisotropy axes are collinear (along z). Details of the Hamiltonians and their interrelationship are discussed in the ESI†.

When comparing Hamiltonians eqn (1) and (2) it becomes obvious that the anisotropic exchange interaction in the spin-1/2 Hamiltonian is a consequence of the formalism when descending from the excited-state Hamiltonian to the spin-1/2 Hamiltonian. In other words, an isotropic exchange coupling in the excited-state Hamiltonian together with the strong 4f anisotropy leads to an anisotropic exchange coupling in the spin-1/2 Hamiltonian. It is, however, not possible to perform this reasoning in the backward sense: if an anisotropic exchange interaction is observed in an effective spin-1/2 model, it is not clear *a priori*, whether this interaction will be isotropic or not in the excited-state Hamiltonian.

Fits using the spin-1/2 Hamiltonian

The spin-1/2 Hamiltonian eqn (2) was least-squares fitted to the experimental Cr and Dy element-specific magnetisation curves and, simultaneously, to the cluster magnetisation curves obtained by SQUID measurements. Here, both Dy centres were treated identically, $\mathbf{g}_{13,\mathrm{eff}} = \mathbf{g}_{1,\mathrm{eff}} = \mathbf{g}_{3,\mathrm{eff}}$, $\mathbf{j}_{\mathrm{eff}} = \mathbf{j}_{12,\mathrm{eff}} = \mathbf{j}_{23,\mathrm{eff}}$, and $\mathbf{j}_{13,\mathrm{eff}}$ and D_2 were set to zero to avoid overparameterisation. It was impossible to obtain a good fit with an Ising-only system, *i.e.* with $g_{13,\mathrm{eff},xy} = 0$, $j_{\mathrm{eff},xy} = 0$ cm^{-1} and $g_{13,\mathrm{eff},z}$ and $j_{\mathrm{eff},z}$ free to vary. In contrast, when $g_{13,\mathrm{eff},xy}$ and $j_{\mathrm{eff},xy}$ were allowed to assume nonzero values, the data could be excellently reproduced. The best-fit curves are shown as black solid lines in Fig. 4. The **j**-matrix anisotropy was linked to that of the **g**-matrix using eqn (S5a)†. The best-fit parameters are

$g_{13,\mathrm{eff},xy} = 5.7(5)$ (free)
$g_{13,\mathrm{eff},z} = 16.3(4)$ (free)
$j_{\mathrm{eff},z} = -2.8(1)$ cm^{-1} (free)
$j_{\mathrm{eff},xy} = -0.98$ cm^{-1} (calculated from free parameters with eqn (S5a)†).

Clearly, $g_{13,\mathrm{eff},z}$ is less than 20.0 which would correspond to a $m_{13,\mathrm{GS}} = \pm 15/2$ ground-state doublet. Hence, this result indicates that the ground-state doublets are characterised by $|m_{13,\mathrm{GS}}| < 15/2$ and/or there is significant admixture of doublets because of non-uniaxial terms, not taken into account in Hamiltonians 1 and 2. Model eqn (2) obviously works in an excellent manner for reproducing all magnetisation data. However, by construction it is only valid at low temperatures and, in addition, the Dy $\mathbf{g}_{\mathrm{eff}}$-matrices and exchange couplings $\mathbf{j}_{ik,\mathrm{eff}}$ are effective quantities. This means that the magnetic parameters in eqn (2) that would allow for the comparison to theoretical values or other models are somewhat hidden.

Fits using the excited-state Hamiltonian

To improve the modelling, the first excited Kramers doublets are also taken into account using the excited-state Hamiltonian eqn (1). In the following we will show that this model is consistent with all our measurements on **1**. We have performed simultaneous least-squares fits of the excited-state Hamiltonian eqn (1) to the element-specific and cluster magnetisation obtained from XMCD and SQUID, respectively, as well as to the dc susceptibility. The separation of the excited state of Dy(1) was fixed to $\delta_1 = 53$ cm^{-1} by choosing D_1 and d_1 accordingly and a minor uniaxial anisotropy on the Cr site $D_2 = -0.52$ cm^{-1} (fixed) was introduced to simultaneously match the INS data, for reasons detailed below. The Cr g-factor was fixed to $g_S = 2$. The only fully independent parameters in this fit were the isotropic exchange couplings $j = j_{12} = j_{23}$ and j_{13} and the isotropic Dy g-factors $g_{13} = g_1 = g_3$. When both Dy^{III} centres where treated identically, no good fit could be obtained. Therefore, we tried different combinations of $\pm 11/2$, $\pm 13/2$, and $\pm 15/2$ ground and excited states by fixing the ground and excited-state doublets and determining the best-fit values. We found best agreement with the data when the ground state of Dy(1) was $m_{1,\mathrm{GS}} = \pm 13/2$, its excited state was $m_{1,\mathrm{ES}} = \pm 15/2$ and the ground state of Dy(3) was $m_{3,\mathrm{GS}} = \pm 15/2$. When the ground-state $|m_{i,\mathrm{GS}}|$ of at least one of the Dy ions was less than 13/2, the calculated dc susceptibility was too low compared to the measured one. Also, adding the first-excited state of Dy(3) did not improve the fits. Therefore, only the ground-state doublet of Dy(3) was taken into account. The corresponding scenario is sketched in Fig. 8a.

The best-fit parameters are:
$\delta_1 = 53.0$ cm^{-1} (fixed)
$D_2 = -0.52$ cm^{-1} (fixed)
$j_{12} = j_{23} = -0.18(3)$ cm^{-1} (free)
$j_{13} = -0.011(4)$ cm^{-1} (free)
$g_{13} = 1.39(5)$ (free).

Here, the extracted g-factor g_{13} is consistent with the value of $g_J = 4/3$. The Dy–Cr exchange coupling is rather weak, but very typical for 3d–4f clusters. Further, the coupling strength between Dy ions j_{13} is close to what is expected from through-space

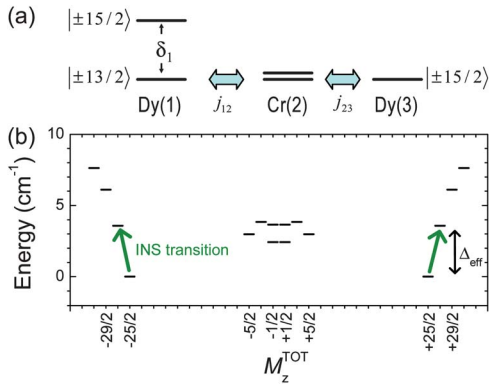

Fig. 8 (a) Scheme of the single-ion energy levels involved in the simulations using the excited-state Hamiltonian eqn (1). (b) Diagram depicting the lowest energy levels of **1** obtained by full diagonalisation of the excited-state Hamiltonian eqn (1) using the best-fit parameters given in the text. The value of the total M_z quantum number is used as x-axis. INS transitions are indicated as green arrows and the effective energy barrier from μSR measurements is shown as a black arrow.

interaction. The calculated χT product using these parameters is drawn as a solid black line in Fig. 5. The simulated INS spectra are shown in Fig. 7c and 7d, demonstrating excellent agreement with the experimental data.

When performing the INS simulations we noticed that a small uniaxial anisotropy on the Cr site of $D_2 = -0.52$ cm^{-1} was necessary to accurately match both INS and XMCD results simultaneously. D_2 mainly leads to a small shift of the INS feature I towards higher energy transfers. Furthermore, we observed that a strong INS transition appears at an energy transfer approximately equal to the separation δ_1. As the fitting results improved with decreasing δ_1, but no strong, magnetic INS transition other than INS peak I was observed, we fixed the separation to $\delta_1 = 53.0$ cm^{-1} which is a value higher than the maximum energy loss of all our INS data. Whereas the high-energy measurements are excellently reproduced, the fine structure observed in Fig. 7b is not captured in full detail. As indicated earlier in the text, the fine structure splitting is in the sub-Kelvin range, implying that it is caused by very weak effects. The introduction of a biaxial anisotropy on the Cr^{III} site or the consideration of unequal exchange couplings $j_{12} \neq j_{23}$ did not allow us to satisfactorily reproduce this fine structure. A possible source of the fine structure could be a non-collinear arrangement of the main anisotropy axes of the three ions. However, although these fine details could not be fully reproduced, certainly the major terms that govern the magnetism of **1** are implemented in our model.

As a result of the restricted basis set, the spectrum of the excited-state Hamiltonian ends at an energy of ~60 cm^{-1}. Any possible higher-energy levels are not taken into account implying that accurate results can be obtained with Hamiltonian eqn (1) for temperatures lower than ~50 K. This is clearly visible in the fit to the dc magnetic susceptibility in Fig. 5.

Density-functional theory

Density-functional theory (DFT) and quantum chemical calculations of 3d–4f systems have been reported on Gd^{III}–M(3d) dimers,[28a,32] whereas the present study is, to the best of our knowledge, the first reporting a DFT calculation on a 3d–4f molecular cluster with a nonzero orbital momentum ground state.

Geometrical optimisation of the truncated model cluster on the (Perdew–Wang) GGA level in scalar-relativistic approximation using a planewave pseudopotential approach[33] well reproduces the molecular structure (for details see ESI†). The GGA-predicted ground-state spin values are $S = 3/2$ (Cr) and $S = 5/2$ (Dy), the latter value is consistent with what is expected for a Dy^{III} ion. A value for the orbital angular momentum is not provided in the scalar-relativistic approximation. Using a scalar-relativistic atom-centred localized basis set approach with a modern hybrid functional (M06-2X),[34] a spin magnetic moment of the Cr^{III} ion of -3.0 μ_B is obtained which is aligned antiparallel to the Dy spin moment of 5.0 μ_B. This ferrimagnetic state is consistent with the XMCD measurements at low magnetic fields. The computed exchange coupling is $j = -40.83$ cm^{-1} with the Ginsberg–Noodleman–Davidson expression[35] and -32.66 cm^{-1} with the expression of Ruiz *et al.*[36] for the experimental crystal structure. Details about the calculations can be found in the ESI†. Note that the mapping of the DFT calculations to the spin Hamiltonian is based on spin-only values S^2 or $S(S + 1)$ (see ESI†). Obviously, the DFT calculations overestimate the exchange coupling. This could be related to a spurious influence of the self-interaction error which will make the Dy 4f orbitals less localised, or it could be related to an influence of the spin–orbit interaction.

The hybrid-functional computed spin densities and the spin polarisation for the ferromagnetic state of the truncated structure are shown in Fig. 9. Here, significant spin polarisation is seen on the magnetic ions but there is also some on the O ligands of Dy, the N ligands of Cr and the bridging fluoride. Importantly, the alternating positive/negative spin polarisation on the latter indicates superexchange interaction. Further, the polarisation of the Cr^{III} ion creates opposite, induced polarisation on its N ligands. In contrast, the parallel orientation of the Dy–O polarization can only be explained by a charge delocalization from Dy to O.

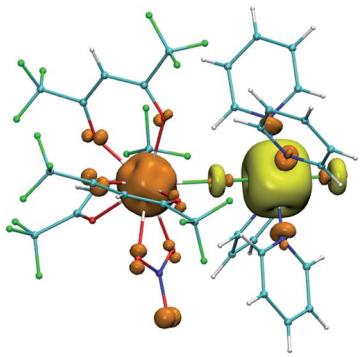

Fig. 9 Spin-density isosurface computed for the zero-field antiferromagnetic state of the truncated model cluster as described in the text. Positive (negative) spin polarisation is plotted as orange (yellow) color. Note that the alternating spin polarisation on the bridging fluoride ion is typical for superexchange.

Discussion

From the element-specific magnetisation curves obtained from XMCD as shown in Fig. 4a and 4b the arrangement of the magnetic moments can be directly read off: Obviously the Dy magnetic moments are close to saturation at a field of $B = 1$ T, indicating a large magnetic moment which is aligned parallel to the applied magnetic field. This is what is expected. In stark contrast, the Cr magnetisation curve exhibits a pronounced wiggle shape with a triple-zero crossing, and only at high magnetic fields it shows the onset of saturation, close to a value of $m_{sat,Cr} = 3\ \mu_B$ consistent with $S_2 = 3/2$ and $g_S = 2$. The wiggle shape implies that at low magnetic fields, the Cr moment is aligned antiparallel to the field and thus to the Dy moments. This behaviour results from the weak antiferromagnetic coupling between the Dy^{III} and Cr^{III} ions observed in **1**: At low magnetic fields it is energetically favourable for the total cluster to assume a ferrimagnetic spin alignment, whereas at high magnetic fields the Zeeman energy overcomes the exchange-coupling energy and the total-cluster energy can be minimised by reversing the Cr spin, leading to a ferromagnetic configuration.

To illustrate the underlying effect of the weak exchange coupling we have performed simulations using the effective spin-1/2 Hamiltonian eqn (2). Here, the Dy^{III} ions were treated identically, $\mathbf{g}_{13,eff} = \mathbf{g}_{1,eff} = \mathbf{g}_{3,eff}$, $\mathbf{j}_{eff} = \mathbf{j}_{12,eff} = \mathbf{j}_{23,eff}$, and $\mathbf{j}_{13,eff} = 0$. The simplified assumptions were $g_{13,eff,xy} = 0$ and $j_{eff,xy} = 0$ cm^{-1}, and the z-components of the Dy $\mathbf{g}_{eff}$ matrices were $g_{13,eff,z} = 20.0$, implying a ground-state Kramers doublet of $m_{13,GS} = \pm 15/2$. The results for different values of $j_{eff,z}$ are shown in Fig. 10. While the Dy magnetisation curves are only weakly dependent on the choice of $j_{eff,z}$, the Cr magnetisation is dramatically affected, delivering a good measure of the exchange coupling.

In addition, we observed that indeed a quite accurate value of the exchange coupling $j = j_{12} = j_{23}$ in the more complex Hamiltonian eqn (1) can be deduced from the simple relation $j_{12} = j_{12,eff,z}\, g_J/g_{13,eff,z}$ obtained from eqn (S5b) and (S5c)†. Using the effective values $j_{12,eff,z}$ and $g_{13,eff,z}$ obtained from the spin-1/2 Hamiltonian fits to the magnetisation curves, we calculate the non-effective exchange coupling (in Hamiltonian eqn (1)) to be $j_{12} = -0.23$ cm^{-1}. This value is very close to that found by the more detailed analysis involving INS and dc magnetic susceptibility suggesting that XMCD data alone can provide sufficient experimental evidence for the extraction of the Dy–Cr exchange coupling in simple clusters. The further agreement with INS and SQUID results underline the strength of the modelling.

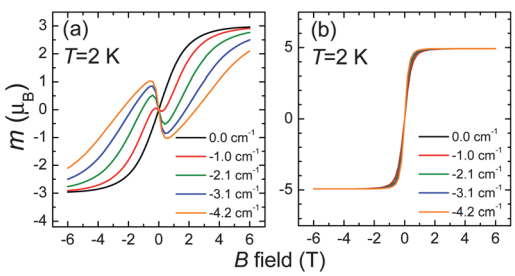

Fig. 10 Simulation of the element-specific magnetisation curves of Cr (a) and Dy (b) using the effective spin-1/2 Hamiltonian eqn (2) with different coupling strengths $j_{eff,z}$ as indicated in the plots. Other parameters are given in the text.

The INS and μSR results can be further understood by using the low-energy spectrum plotted in Fig. 8b. Here, the total-spin m_s value $M_z^{TOT} = \langle n|\sum \hat{S}_{i,z}|n\rangle$ is used as x-axis. The spectrum was obtained by full diagonalisation of the excited-state Hamiltonian eqn (1) using the best-fit parameters. The ground states are characterised by a $|\pm 25/2\rangle$ doublet reflecting the ferrimagnetic arrangement of the Dy and Cr magnetic moments. The INS transition I is indicated by green arrows and a black arrow shows the height of the effective energy barrier of $\Delta_{eff} = 3.0$ cm^{-1} obtained by μSR. This barrier height can be explained by considering small non-uniaxial terms in the excited-state Hamiltonian. In the simplest case, this could be a cluster E (biaxial anisotropy) term. In general, such a term is able to mix energy eigenstates with $\Delta M_z^{TOT} = \pm 2k$ with integer k, and regarding the spectrum of **1** it would be weakly allowed that the $|\pm 25/2\rangle$ ground states mix with the excited $|\mp 27/2\rangle$ states located at an energy of 3.6 cm^{-1}. Such a mixing would give rise to quantum tunnelling of the magnetisation through the excited states, explaining the observed temperature dependence of the relaxation time and the low effective barrier for magnetization reversal.

As aforementioned, the DFT calculations are successful in reproducing the molecular geometry of the truncated model system and the sign of the magnetic exchange coupling. Fig. 9 reveals that the bridging fluoride ion which mediates the Dy–Cr interaction is spin-polarised in an alternating positive/negative fashion substantiating that superexchange is at the origin of the antiferromagnetic exchange coupling. Although the ligand spin polarisation may appear large in the spin-polarisation map, it is only on the order of 0.03 μ_B. Therefore it is justified to neglect it in the spin-Hamiltonian analysis.

Conclusions

We have reported the syntheses and crystal structures of two novel 3d–4f clusters containing Dy and Cr featuring linear, unsupported fluoride bridges. Further, we have performed an in-depth study of the magnetism of the trinuclear compound **1**. The element-specific magnetisation curves obtained from XMCD directly reveal the field-induced transition from the ferrimagnetic to the ferromagnetic alignments of the Dy and Cr magnetic moments. Our findings are corroborated by SQUID magnetometry and INS which confirm the isotropic Dy–Cr exchange coupling of $j = -0.18$ cm^{-1} obtained from XMCD. The μSR and ac susceptibility measurements suggest that **1** is a SMM with a small effective barrier $\Delta_{eff} = 3$ cm^{-1}. We have successfully modelled the data using spin-Hamiltonian models at different levels of complexity. The DFT calculations reveal spin polarisation on the Dy and Cr ligands and suggest that the antiferromagnetic Dy–Cr coupling originates from superexchange *via* the fluoride ion bridge.

Our results demonstrate that XMCD is suitable to determine the sign and strength of the weak exchange coupling between Dy and Cr ions. This mitigates the problem that in such 3d–4f compounds often the information about intracluster magnetic couplings contained in the temperature-dependent magnetic susceptibility is concealed by the much stronger effect of the 4f-anisotropy splittings. As this scenario can be expected to be

realised in most 3d–4f compounds, our approach may be applicable to a large number of oligonuclear 3d–4f compounds.

Notes and references

1 (*a*) A. Caneschi, D. Gatteschi, R. Sessoli, A. L. Barra, L. C. Brunel and M. Guillot, *J. Am. Chem. Soc.*, 1991, **113**, 5873; (*b*) R. Sessoli, D. Gatteschi, A. Caneschi and M. A. Novak, *Nature*, 1993, **365**, 141; (*c*) D. Gatteschi, A. Caneschi, L. Pardi and R. Sessoli, *Science*, 1994, **265**, 1054; (*d*) G. Christou, D. Gatteschi, D. N. Hendrickson and R. Sessoli, *MRS Bull.*, 2000, **25**, 66; (*e*) C. Cadiou, M. Murrie, C. Paulsen, V. Villar, W. Wernsdorfer and R. E. P. Winpenny, *Chem. Commun.*, 2001, 2666; (*f*) J. J. Sokol, A. G. Hee and J. R. Long, *J. Am. Chem. Soc.*, 2002, **124**, 7656; (*g*) C. J. Milios, A. Vinslava, W. Wernsdorfer, S. Moggach, S. Parsons, S. P. Perlepes, G. Christou and E. K. Brechin, *J. Am. Chem. Soc.*, 2007, **129**, 2754.

2 (*a*) O. Waldmann, *Inorg. Chem.*, 2007, **46**, 10035; (*b*) E. Ruiz, J. Cirera, J. Cano, S. Alvarez, C. Loose and J. Kortus, *Chem. Commun.*, 2008, 52; (*c*) R. Sessoli and A. K. Powell, *Coord. Chem. Rev.*, 2009, **253**, 2328; (*d*) L. Sorace, C. Benelli and D. Gatteschi, *Chem. Soc. Rev.*, 2011, **40**, 3092.

3 (*a*) N. Ishikawa, M. Sugita, T. Ishikawa, S. Koshihara and Y. Kaizu, *J. Am. Chem. Soc.*, 2003, **125**, 8694; (*b*) N. Ishikawa, *Polyhedron*, 2007, **26**, 2147.

4 (*a*) M. A. AlDamen, J. M. Clemente-Juan, E. Coronado, C. Marti-Gastaldo and A. Gaita-Arino, *J. Am. Chem. Soc.*, 2008, **130**, 8874; (*b*) M. A. AlDamen, S. Cardona-Serra, J. M. Clemente-Juan, E. Coronado, A. Gaita-Arino, C. Marti-Gastaldo, F. Luis and O. Montero, *Inorg. Chem.*, 2009, **48**, 3467.

5 S.-D. Jiang, B.-W. Wang, H.-L. Sun, Z.-M. Wang and S. Gao, *J. Am. Chem. Soc.*, 2011, **133**, 4730.

6 R. Giraud, W. Wernsdorfer, A. M. Tkachuk, D. Mailly and B. Barbara, *Phys. Rev. Lett.*, 2001, **87**, 057203.

7 (*a*) P.-H. Lin, T. Burchell, L. Ungur, L. Chibotaru, W. Wernsdorfer and M. Murugesu, *Angew. Chem., Int. Ed.*, 2009, **48**, 9489; (*b*) I. J. Hewitt, J. Tang, N. T. Madhu, C. E. Anson, Y. Lan, J. Luzon, M. Etienne, R. Sessoli and A. K. Powell, *Angew. Chem., Int. Ed.*, 2010, **49**, 6352; (*c*) Y.-N. Guo, G.-F. Xu, P. Gamez, L. Zhao, S.-Y. Lin, R. Deng, J. Tang and H.-J. Zhang, *J. Am. Chem. Soc.*, 2010, **132**, 8538; (*d*) R. J. Blagg, C. A. Muryn, E. J. L. McInnes, F. Tuna and R. E. P. Winpenny, *Angew. Chem., Int. Ed.*, 2011, **50**, 6530; (*e*) J. Long, F. Habib, P.-H. Lin, I. Korobkov, G. Enright, L. Ungur, W. Wernsdorfer, L. F. Chibotaru and M. Murugesu, *J. Am. Chem. Soc.*, 2011, **133**, 5319.

8 (*a*) J. D. Rinehart, M. Fang, W. J. Evans and J. R. Long, *Nat. Chem.*, 2011, **3**, 538; (*b*) J. D. Rinehart, M. Fang, W. J. Evans and J. R. Long, *J. Am. Chem. Soc.*, 2011, **133**, 14236.

9 (*a*) C. M. Zaleski, E. C. Depperman, J. W. Kampf, M. L. Kirk and V. L. Pecoraro, *Angew. Chem., Int. Ed.*, 2003, **43**, 3912; (*b*) S. Osa, T. Kido, N. Matsumoto, N. Re, A. Pochaba and J. Mrozinski, *J. Am. Chem. Soc.*, 2004, **126**, 420; (*c*) A. Mishra, W. Wernsdorfer, K. A. Abboud and G. Christou, *J. Am. Chem. Soc.*, 2004, **126**, 15648; (*d*) F. Mori, T. Ishida and T. Nogami, *Polyhedron*, 2005, **24**, 2588; (*e*) J. P. Costes, F. Dahan and W. Wernsdorfer, *Inorg. Chem.*, 2006, **45**, 5; (*f*) C. Aronica, G. Pilet, G. Chastanet, W. Wernsdorfer, J. F. Jacquot and D. Luneau, *Angew. Chem., Int. Ed.*, 2006, **45**, 4659; (*g*) V. Mereacre, A. M. Ako, R. Clerac, W. Wernsdorfer, I. J. Hewitt, C. E. Anson and A. K. Powell, *Chem.–Eur. J.*, 2008, **14**, 3577; (*h*) J. Rinck, G. Novitchi, W. Van den Heuvel, L. Ungur, Y. Lan, W. Wernsdorfer, C. E. Anson, L. F. Chibotaru and A. K. Powell, *Angew. Chem., Int. Ed.*, 2010, **49**, 7583; (*i*) M. Hołyńska, D. Premužić, I.-R. Jeon, W. Wernsdorfer, R. Clérac and S. Dehnen, *Chem.–Eur. J.*, 2011, **17**, 9605.

10 W. W. Lukens and M. D. Walter, *Inorg. Chem.*, 2010, **49**, 4458.

11 (*a*) N. Ishikawa, M. Sugita, T. Okubo, N. Tanaka, T. Iino and Y. Kaizu, *Inorg. Chem.*, 2003, **42**, 2440; (*b*) J. Luzon, K. Bernot, I. J. Hewitt, C. E. Anson, A. K. Powell and R. Sessoli, *Phys. Rev. Lett.*, 2008, **100**, 247205.

12 (*a*) G. van der Laan and B. T. Thole, *Phys. Rev. B: Condens. Matter*, 1991, **43**, 13401; (*b*) J. Stöhr, *J. Magn. Magn. Mater.*, 1999, **200**, 470; (*c*) T. Funk, A. Deb, S. J. George, H. Wang and S. P. Cramer, *Coord. Chem. Rev.*, 2005, **249**, 3.

13 (*a*) M.-A. Arrio, A. Scuiller, P. Sainctavit, C. Cartier dit Moulin, T. Mallah and M. Verdaguer, *J. Am. Chem. Soc.*, 1999, **121**, 6414; (*b*) G. Champion, N. Lalioti, V. Tangoulis, M.-A. Arrio, P. Sainctavit, F. Villain, A. Caneschi, D. Gatteschi, C. Giorgetti, F. Baudelet, M. Verdaguer and C. Cartier dit Moulin, *J. Am. Chem. Soc.*, 2003, **125**, 8371; (*c*) R. Moroni, C. Cartier dit Moulin, G. Champion, M.-A. Arrio, P. Sainctavit, M. Verdaguer and D. Gatteschi, *Phys. Rev. B: Condens. Matter*, 2003, **68**, 064407; (*d*) T. Hamamatsu, K. Yabe, M. Towatari, S. Osa, N. Matsumoto, N. Re, A. Pochaba, J. Mrozinski, J. L. Gallani, A. Barla, P. Imperia, C. Paulsen and J. P. Kappler, *Inorg. Chem.*, 2007, **46**, 4458; (*e*) M. Mannini, F. Pineider, P. Sainctavit, C. Danieli, E. Otero, C. Sciancalepore, A. M. Talarico, M.-A. Arrio, A. Cornia, D. Gatteschi and R. Sessoli, *Nat. Mater.*, 2009, **8**, 194; (*f*) G. Rogez, B. Donnio, E. Terazzi, J.-L. Gallani, J.-P. Kappler, J.-P. Bucher and M. Drillon, *Adv. Mater.*, 2009, **21**, 4323; (*g*) P. Gambardella, S. Stepanow, A. Dmitriev, J. Honolka, F. M. F. de Groot, M. Lingenfelder, S. Sen Gupta, D. D. Sarma, P. Bencok, S. Stanescu, S. Clair, S. Pons, N. Lin, A. P. Seitsonen, H. Brune, J. V. Barth and K. Kern, *Nat. Mater.*, 2009, **8**, 189; (*h*) R. Biagi, J. Fernandez-Rodriguez, M. Gonidec, A. Mirone, V. Corradini, F. Moro, V. De Renzi, U. del Pennino, J. C. Cezar, D. B. Amabilino and J. Veciana, *Phys. Rev. B: Condens. Matter Mater. Phys.*, 2010, **82**, 224406; (*i*) S. Stepanow, J. Honolka, P. Gambardella, L. Vitali, N. Abdurakhmanova, T.-C. Tseng, S. Rauschenbach, S. L. Tait, V. Sessi, S. Klyatskaya, M. Ruben and K. Kern, *J. Am. Chem. Soc.*, 2010, **132**, 11900; (*j*) M. Prinz, K. Kuepper, C. Taubitz, M. Raekers, S. Khanra, B. Biswas, T. Weyhermüller, M. Uhlarz, J. Wosnitza, J. Schnack, A. V. Postnikov, C. Schröder, S. J. George, M. Neumann and P. Chaudhuri, *Inorg. Chem.*, 2010, **49**, 2093; (*k*) V. Corradini, A. Ghirri, U. del Pennino, R. Biagi, V. A. Milway, G. Timco, F. Tuna, R. E. P. Winpenny and M. Affronte, *Dalton Trans.*, 2010, **39**, 4928; (*l*) M. Gonidec, R. Biagi, V. Corradini, F. Moro, V. De Renzi, U. del Pennino, D. Summa, L. Muccioli, C. Zannoni, D. B. Amabilino and J. Veciana, *J. Am. Chem. Soc.*, 2011, **133**, 6603; (*m*) M. Mannini, E. Tancini, L. Sorace, P. Sainctavit, M.-A. Arrio, Y. Qian, E. Otero, D. Chiappe, L. Margheriti, J. C. Cezar, R. Sessoli and A. Cornia, *Inorg. Chem.*, 2011, **50**, 2911; (*n*) A. Lodi Rizzini, C. Krull, T. Balashov, J. J. Kavich, A. Mugarza, P. S. Miedema, P. K. Thakur, V. Sessi, S. Klyatskaya, M. Ruben, S. Stepanow and P. Gambardella, *Phys. Rev. Lett.*, 2011, **107**, 177205.

14 (*a*) M. T. Gamer, Y. Lan, P. W. Roesky, A. K. Powell and R. Clérac, *Inorg. Chem.*, 2008, **47**, 6581; (*b*) R. Bircher, B. F. Abrahams, H. U. Güdel and C. Boskovic, *Polyhedron*, 2007, **26**, 3023; (*c*) L. G. Westin, M. Kristikos and A. Caneschi, *Chem. Commun.*, 2003, 1012; (*d*) T. Kajiwara, K. Katagiri, S. Takaishi, M. Yamashita and N. Iki, *Chem.–Asian J.*, 2006, **1**, 349.

15 (*a*) F. Pointillart, K. Bernot and R. Sessoli, *Inorg. Chem. Commun.*, 2007, **10**, 471; (*b*) F. Pointillart, K. Bernot, R. Sessoli and D. Gatteschi, *Inorg. Chem.*, 2010, **49**, 4355; (*c*) P.-H. Lin, I. Korobkov, W. Wernsdorfer, L. Ungur, L. F. Chibotaru and M. Murugesu, *Eur. J. Inorg. Chem.*, 2011, 1535.

16 (*a*) T. Birk, K. S. Pedersen, S. Piligkos, C. A. Thuesen, H. Weihe and J. Bendix, *Inorg. Chem.*, 2011, **50**, 5312; (*b*) T. Birk, M. J. Magnussen, S. Piligkos, H. Weihe, A. Holten and J. Bendix, *J. Fluorine Chem.*, 2010, **131**, 898.

17 F. Perdih, A. Demsar, A. Pevec, S. Petricek, I. Leban, G. Giester, J. Sieler and H. W. Roesky, *Polyhedron*, 2001, **20**, 1967.

18 A. Pevec, M. Mrak, A. Demsar, S. Petricek and H. W. Roesky, *Polyhedron*, 2003, **22**, 575.

19 A. McRobbie, A. R. Sarwar, S. Yeninas, H. Nowell, M. L. Baker, D. Allan, M. Luban, C. A. Muryn, R. G. Pritchard, R. Prozorov, G. A. Timco, F. Tuna, G. F. S. Whitehead and R. E. P. Winpenny, *Chem. Commun.*, 2011, **47**, 6251.

20 T. Birk, M. Schau-Magnussen, T. Weyhermüller and J. Bendix, *Acta Crystallogr., Sect. E: Struct. Rep. Online*, 2011, **67**, m1561.

21 (*a*) J. Glerup, J. Josephsen, K. Michelsen, E. Pedersen and C. E. Schäffer, *Acta Chem. Scand.*, 1970, **24**, 247; (*b*) P. Andersen, A. Døssing, J. Glerup and M. Rude, *Acta Chem. Scand.*, 1990, **44**, 346; (*c*) A. Böttcher, H. Elias, J. Glerup, M. Neuburger, C. E. Olsen, H. Paulus, J. Springborg and M. Zehnder, *Acta Chem. Scand.*, 1994, **48**, 967; (*d*) A. Böttcher, H. Elias, J. Glerup, M. Neuburger, C. E. Olsen, J. Springborg, H. Weihe and M. Zehnder, *Acta Chem. Scand.*, 1994, **48**, 981.

22 G. Fochi, J. Strähle and F. Gingl, *Inorg. Chem.*, 1991, **30**, 4669.
23 (*a*) B. T. Thole, P. Carra, F. Sette and G. van der Laan, *Phys. Rev. Lett.*, 1992, **68**, 1943; (*b*) P. Carra, B. T. Thole, M. Altarelli and X. Wang, *Phys. Rev. Lett.*, 1993, **70**, 694; (*c*) C. T. Chen, Y. U. Idzerda, H.-J. Lin, N. V. Smith, G. Meigs, E. Chaban, G. H. Ho, E. Pellegrin and F. Sette, *Phys. Rev. Lett.*, 1995, **75**, 152.
24 (*a*) Y. Teramura, A. Tanaka and T. Jo, *J. Phys. Soc. Jpn.*, 1996, **65**, 1053; (*b*) C. Piamonteze, P. Miedema and F. M. F. de Groot, *Phys. Rev. B: Condens. Matter Mater. Phys.*, 2009, **80**, 184410.
25 (*a*) T. Lancaster, S. J. Blundell, F. L. Pratt, I. Franke, A. J. Steele, P. J. Baker, Z. Salman, C. Baines, I. Watanabe, S. Carretta, G. A. Timco and R. E. P. Winpenny, *Phys. Rev. B: Condens. Matter Mater. Phys.*, 2010, **81**, 140409; (*b*) Z. Salman, S. R. Giblin, Y. Lan, A. K. Powell, R. Scheuermann, R. Tingle and R. Sessoli, *Phys. Rev. B: Condens. Matter Mater. Phys.*, 2010, **82**, 174427.
26 S. Cotton, *Lanthanide and Actinide Chemistry*; John Wiley & Sons, 2006.
27 A. Abragam and B. Bleaney, *Electron Paramagnetic Resonance of Transition Metal Ions*; Dover: New York, 1986.
28 (*a*) J. Paulovic, F. Cimpoesu, M. Ferbinteanu and K. J. Hirao, *J. Am. Chem. Soc.*, 2004, **126**, 3321; (*b*) L. Chibotaru, L. Ungur and A. Soncini, *Angew. Chem., Int. Ed.*, 2008, **47**, 4126; (*c*) K. Bernot, J. Luzon, L. Bogani, M. Etienne, C. Sangregorio, M. Shanmugam, A. Caneschi, R. Sessoli and D. Gatteschi, *J. Am. Chem. Soc.*, 2009, **131**, 5573.
29 *E.g.*, a ground state of $m_i = \pm 15/2$ and a first excited state of $m_i = \pm 13/2$ generate $D_i = -\delta_i/14$ and $d_i = 2\delta_i$.
30 J. Luzon, K. Bernot, I. J. Hewitt, C. E. Anson, A. K. Powell and R. Sessoli, *Phys. Rev. Lett.*, 2008, **100**, 247205.
31 A. Palii, B. Tsukerblat, S. Klokishner, K. R. Dunbar, J. M. Clemente-Juan and E. Coronado, *Chem. Soc. Rev.*, 2011, **40**, 3130, and references therein.
32 (*a*) I. Rudra, C. Raghu and S. Ramasesha, *Phys. Rev. B: Condens. Matter*, 2002, **65**, 224411; (*b*) X.-R. Sun, Z.-D. Chen, M.-W. Wang, B.-W. Wang, F. Yan and K.-K. Cheung, *Chin. J. Chem.*, 2007, **25**, 329; (*c*) G. Rajaraman, F. Totti, A. Bencini, A. Caneschi, R. Sessoli and D. Gatteschi, *Dalton Trans.*, 2009, 3153.
33 (*a*) G. Kresse and J. Hafner, *Phys. Rev. B: Condens. Matter*, 1993, **47**, 558; (*b*) G. Kresse and J. Furthmüller, *Phys. Rev. B: Condens. Matter*, 1996, **54**, 11169; (*c*) P. E. Blöchl, *Phys. Rev. B: Condens. Matter*, 1994, **50**, 17953; (*d*) G. Kresse and J. Furthmüller, *Phys. Rev. B: Condens. Matter*, 1996, **54**, 11169.
34 Y. Zhao and D. Truhlar, *Theor. Chem. Acc.*, 2008, **120**, 215.
35 (*a*) A. P. Ginsberg, *J. Am. Chem. Soc.*, 1980, **102**, 111; (*b*) L. Noodleman, *J. Chem. Phys.*, 1981, **74**, 5737; (*c*) L. Noodleman and E. R. Davidson, *Chem. Phys.*, 1986, **109**, 131.
36 E. Ruiz, J. Cano, S. Alvarez and P. Alemany, *J. Comput. Chem.*, 1999, **20**, 1391.

Electronic Supplementary Information

Direct observation of a ferri-to-ferromagnetic transition in a fluoride-bridged 3d-4f molecular cluster

Jan Dreiser,*[a] Kasper S. Pedersen,*[b] Cinthia Piamonteze,[a] Stefano Rusponi,[c] Zaher Salman,[d] Md. Ehesan Ali,[e] Magnus Schau-Magnussen,[b] Christian Aa. Thuesen,[b] Stergios Piligkos,[b] Høgni Weihe,[b] Hannu Mutka,[f] Oliver Waldmann,[g] Peter Oppeneer,[h] Jesper Bendix,*[b] Frithjof Nolting,[a] and Harald Brune[c]

[a] *Swiss Light Source, Paul Scherrer Institut, CH-5232 Villigen PSI, Switzerland. E-mail: jan.dreiser@psi.ch*

[b] *Department of Chemistry, University of Copenhagen, DK-2100 Copenhagen, Denmark. E-mail: ksp@kiku.dk (K.S.P.), bendix@kiku.dk (J.B.)*

[c] *Institute of Condensed Matter Physics, Ecole Polytechnique Fédérale de Lausanne, CH-1015 Lausanne, Switzerland.*

[d] *Laboratory for Muon Spin Spectroscopy, Paul Scherrer Institut, CH-5232 Villigen PSI, Switzerland.*

[e] *Center for Theoretical Chemistry, Ruhr-Universität Bochum, D-44801, Bochum, Germany.*

[f] *Institut Laue-Langevin, F-38042 Grenoble Cedex 9, France.*

[g] *Physikalisches Institut, Universität Freiburg, D-79104 Freiburg, Germany.*

[h] *Department of Physics and Astronomy, Uppsala University, Box 516, S-751 20 Uppsala, Sweden.*

.

Table of contents

Experimental Section

General Procedures and Materials

All chemicals and solvents were purchased from commercial sources and used without further purification. $[Dy(hfac)_3(H_2O)_2]$ and *trans*-$[CrF_2(py)_4]NO_3$ were prepared as described in the literature.[1]

Syntheses

Synthesis of 1: To a solution of $[Dy(hfac)_3(H_2O)_2]$ (4.0 g, 4.9 mmol) in chloroform (60 ml, LabScan; stabilized by 1% ethanol) was added a solution of *trans*-$[CrF_2(py)_4]NO_3$ (0.5 g, 1.0 mmol) in chloroform (10 ml). The resulting solution was left standing for 12 h to yield needles of $[Dy(hfac)_3(H_2O)–CrF_2(py)_4–Dy(hfac)_3(NO_3)]$ which were filtered off and washed with chloroform. Yield: 62% (based on Cr). *Anal. Calc.* (found) for $H_{28}C_{50}N_5O_{16}F_{38}CrDy_2$: C: 29.24% (29.13%), H: 1.37% (1.26%), N: 3.41% (3.33%)

Synthesis of 2: To a solution of *trans*-$[CrF_2(py)_4]NO_3$ (1.2 g, 2.6 mmol) in chloroform (25 ml) was added a solution of one equivalent $[Dy(hfac)_3(H_2O)_2]$ (2.1 g, 2.6 mmol) in chloroform (40 ml). Red-violet, block-shaped crystals of $[Dy(hfac)_4–CrF_2(py)_4]\cdot ½CHCl_3$ were filtered off after several hours and washed with successive aliquots of chloroform. The samples were stored in closed vials in a freezer to suppress solvent loss. Yield: 36% (based on Cr), *Anal. calc.* (found) for $H_{24.5}C_{40.5}N_4O_8F_{26}Cl_{1.5}CrDy$: C: 33.39% (33.02%), H: 1.70% (1.49%), N: 3.85% (3.90%).

Crystallography

Single-crystal X-ray diffraction data were acquired at 122 K on a Nonius KappaCCD area-detector diffractometer, equipped with an Oxford Cryostreams low-temperature device, using graphite-monochromated Mo Kα radiation (λ = 0.71073 Å). The structures were solved using direct methods (SHELXS97) and refined using the SHELXL97 software package.[2] All non-hydrogen atoms were refined anisotropically, whereas H-atoms were isotropic and constrained. Crystal structure and refinement data for **1** and **2** are summarised in Table S1. The structure of **2** contains a highly disordered solvent $CHCl_3$ molecule and no satisfactory model that describes this solvent could be achieved. Hence the PLATON SQUEEZE[3] procedure was used in the refinement to calculate a solvent-accessible void of 311 $Å^3$. It was confirmed that the disordered solvent is located in the void volume.

	1	**2**
Formula	$C_{50}H_{28}CrDy_2F_{38}N_5O_{16}$	$C_{40}H_{24}CrDyF_{26}N_4O_8$
M_r	2053.77	1397.13
Color, shape	Pink, prism	Pink, prism
crystal size/mm	0.45 × 0.10 × 0.09	0.36 × 0.18 × 0.09
Crystal system	Monoclinic	triclinic
Space group	*C*2/*c*	P-1
T/K	122	122
a/Å	26.3208 (13)	12.515 (5)
b/Å	15.7874 (15)	19.836 (7)
c/Å	18.718 (3)	21.392 (6)
α/°	90	85.52 (3)
β/°	115.474 (9)	81.35 (4)
γ/°	90	86.229 (19)
V/Å^3	7021.9 (13)	5226 (3)
Z	4	4
ρ_{calc}/g cm^{-3}	1.943	1.776
F_{000}	3956	2720
μ(Mo *K*α)/mm^{-1}	2.42	1.77
θ range/°	1.6–27.5	1.0–35.0
collected reflns	73764	299677
unique reflns	8074	45853
params/restraints	534/3	1441/0
reflns ($I > 2\sigma(I)$)	6301	33140
GoF	1.07	1.04
$R1^a$($I > 2.00\sigma(I)$)	0.041	0.043
$R1^a$(all data)	0.062	0.073
$wR2^b$(all data)	0.107	0.095
max/min $\Delta\rho$/e Å^{-3}	1.56/−0.84	1.69/−1.27

[a] $R1 = \Sigma||F_o| - |F_c||/\Sigma|F_o|$. [b] $wR2 = [\Sigma w(F_o^2 - F_c^2)^2/\Sigma w(F_o^2)^2]^{1/2}$

Table S1: Crystallographic data of **1** and **2**.

SQUID magnetometer measurements

The magnetic characterisation was performed on a Quantum-Design MPMS-XL SQUID magnetometer equipped with a 5 T dc magnet. The polycrystalline samples were enclosed in frozen *n*-eicosane in polycarbonate capsules. The temperature dependence of the dc magnetic susceptibility was determined from magnetisation measurements from 1.8 K to 300 K in a dc field of 100 mT. Magnetisation data were acquired at fields up to 5 T and at different temperatures. Data were

corrected for diamagnetic contributions from the sample, *n*-eicosane and the sample holder by means of Pascal´s constants. Ac susceptibility measurements were carried out using an oscillating field of 0.3 mT and static dc fields of up to 1 T.

X-ray magnetic circular dichroism

X-ray magnetic circular dichroism (XMCD) measurements were performed at the X-Treme beamline at the Swiss Light Source, Paul Scherrer Institut, Switzerland. To prepare the sample, polycrystalline powder of **1** was pressed into a piece of Indium mounted on a sample holder. X-ray absorption spectra were recorded at a temperature of 2 K in total electron yield mode at the Dy $M_{4,5}$ and Cr $L_{2,3}$ edges. Magnetic fields of up to $B = \pm 6$ T along the beam propagation direction were applied. The beam was defocused (spot size $\sim 1 \times 1$ mm^2) and kept at very low intensity to avoid radiation damage. Scans were taken "on-the-fly", i.e. the monochromator and insertion device were moving continuously while the data were acquired.[4] To obtain magnetisation curves, a full magnetic-field loop was performed at one polarisation while measuring X-ray absorption at the energy of maximum dichroism and at the baseline. Hereafter, the polarisation was changed and another loop was run.

Muon-spin relaxation

The μSR measurements were performed on the GPS spectrometer at the Paul Scherrer Institute in Switzerland. In these experiments spin-polarised positive muons are implanted in the sample. Each implanted muon decays (lifetime 2.2 μsec) emitting a positron preferentially in the direction of its spin polarisation at the time of decay. Using appropriately positioned detectors, one measures the asymmetry of positron emission as a function of time, $A(t)$, which is proportional to the time evolution of the muon spin polarisation. $A(t)$ depends on the distribution of internal magnetic fields and their temporal fluctuations. Further details on the μSR technique may be found in ref. 5.

Inelastic neutron scattering

Inelastic neutron scattering (INS) experiments were carried out using the direct-geometry time-of-flight neutron spectrometer IN5 located at the Institut Laue-Langevin, Grenoble, France. Approximately 1 g of crystalline material was loaded into a 10 mm-diameter double-wall, hollow aluminum cylinder. Spectra were acquired with incident neutron wavelengths of 3 Å, 4.8 Å and 6.5 Å at temperatures from 1.5 K to 15 K. The detector efficiency correction was performed using data collected from Vanadium and the background was subtracted. The data were processed and analysed using the LAMP program package.[6]

Density-functional theory calculations

Density-functional theory (DFT) calculations were performed on two levels of sophistication. To investigate the exchange coupling in complex **1** we considered the truncated model cluster [Dy(hfac)$_3$(NO$_3$)–CrF$_2$(py)$_4$]. Geometrical optimisation of this model cluster was performed using the VASP full-potential plane-wave code in scalar-relativistic approximation, in which pseudo-potentials together within the projector augmented wave method are used.[7] A kinetic energy cutoff of 400 eV was employed for the plane waves. For the DFT exchange-correlation functional the generalised gradient approximation (GGA) in the Perdew-Wang parameterisation[8] was used for the geometrical optimisation. A cubic simulation box of 30×30×30 Å^3 and the Γ point in reciprocal space were used. The magnetic properties of the optimised geometries as well as the experimental crystallographic structure were furthermore investigated using the atom-centered localized basis set approach as implemented in the NWChem package[9] in combination with hybrid functionals. In the latter calculations the segmented all-electron relativistic contracted basis sets for zeroth-order regular approximation (SARC-ZORA)[10] scalar-relativistic Hamiltonians were used for Dy and all-electron 6-31G* basis sets for all other atoms including Cr.

Isotropic magnetic exchange interactions were calculated within the localised basis set approach, using the hybrid meta-GGA M06-2X functional[11] in combination with applying the spin-polarized broken symmetry approach. The magnetic interaction of the model complex was expressed as $\hat{H} = -j\hat{\mathbf{S}}_{\mathrm{Dy}} \cdot \hat{\mathbf{S}}_{\mathrm{Cr}}$ where the exchange constant j can be extracted from the Noodleman-Ginsberg-Davidson expression[12] $j=2(E_{\mathrm{BS}}-E_{\mathrm{HS}})/S_{\mathrm{max}}^2$ (with E_{BS} the broken-symmetry energy and E_{HS} the high-symmetry energy). In the literature an alternative expression by Ruiz et al.[13] [$j=2(E_{\mathrm{BS}}-E_{\mathrm{HS}})/S_{\mathrm{max}}(S_{\mathrm{max}}+1)$] is popular and provides computationally better results in most cases. However no theoretical basis to prefer Ruiz et al.'s expression over the other one was established so far, therefore both expressions were explored here.

Spin-Hamiltonian simulations and fits

The spin-Hamiltonian simulations used to reproduce local and cluster magnetization curves, dc magnetic susceptibility and INS spectra are based on full diagonalization of the respective Hamiltonians. To take into account the powder nature of the sample, local and cluster magnetization curves were averaged over different directions of the magnetic field according to the equation

$$m_{i,\,\mathrm{powder}}(B) = \frac{1}{4\pi} \int_{\theta,\phi} \mathbf{m}_i(B,\theta,\phi) \cdot \mathbf{n}(\theta,\phi) \sin\theta \, d\theta \, d\phi \qquad \text{(S1)}$$

Here, $\mathbf{m}_i$ is the magnetic moment of element i, depending on the magnitude and orientation of the applied magnetic field which is expressed in spherical coordinates $\mathbf{B} = (B,\theta,\phi)$. Further, $\mathbf{n}$ is the unit

vector pointing along the *B*-field direction. This integral was realized numerically using a 16-point Lebedev-Laikov grid.[14] All fits shown in this work are least-squares fits which were obtained by minimizing the sum of squared deviations between the measured and calculated curves. The calculations were performed using home-written Matlab® and C codes.

Supplementary Information to the Results Section of the Main Article

Crystallography: Thermal ellipsoid plots of the crystal structures of 1 and 2

These plots indicate the thermal motion of the atoms in a molecule. Magnitude and anisotropy of the vibrations are coded as size and shape of the ellipsoids.

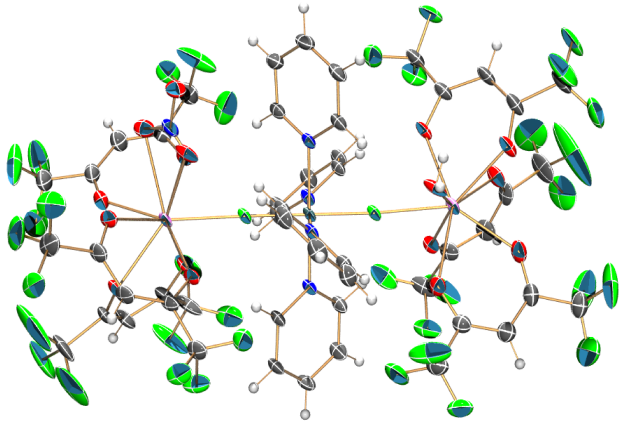

Fig. S1 Thermal ellipsoid plot (30% probability level) of **1**. Color code: pink: Dy, dark green: Cr, light green: F, red: O, blue: N, white: H.

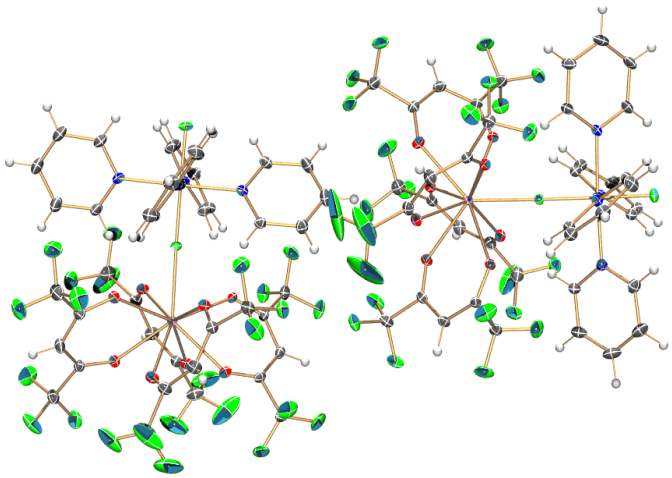

Fig. S2 Thermal ellipsoid plot (30% probability level) of **2**. Color code: pink: Dy, dark green: Cr, light green: F, red: O, blue: N, white: H.

X-ray absorption spectroscopy

XMCD is obtained following $I_{\mathrm{XMCD}}(E) = I_{+}(E) - I_{-}(E)$ where I_{+} and I_{-} refer to the X-ray absorption intensities for the two circular polarisations of the X-rays. The XMCD sum rules are given by[15]

$$\frac{\int_{\mathrm{M}_{4,5}} \mathrm{d}\omega(\mu^{+}-\mu^{-})}{\int_{\mathrm{M}_{4,5}} \mathrm{d}\omega(\mu^{+}+\mu^{-}+\mu^{0})} = \frac{1}{2}\frac{l(l+1)+2-c(c+1)}{l(l+1)(4l+2-n)}\langle L_z\rangle \qquad \text{(S2)}$$

$$\frac{\int_{\mathrm{M}_5} \mathrm{d}\omega(\mu^{+}-\mu^{-}) - \frac{c+1}{c}\int_{\mathrm{M}_4} \mathrm{d}\omega(\mu^{+}-\mu^{-})}{\int_{\mathrm{M}_{4,5}} \mathrm{d}\omega(\mu^{+}+\mu^{-}+\mu^{0})} = \frac{l(l+1)-2-c(c+1)}{3c(4l+2-n)}\langle S_z\rangle + \frac{l(l+1)[l(l+1)+2c(c+1)+4\,]-3(c-1)^2(c+2)^2}{6lc(l+1)(4l+2-n)}\langle T_z\rangle \qquad \text{(S3)}$$

Here, c, l and n denote the orbital quantum number of the core and the valence shell involved in the X-ray absorption process and the number of electrons in the valence shell, respectively. For the $M_{4,5}$ edges of the Dy^{III} ion, $c = 2$, $l = 3$ and $n = 9$. We replace $A = \int_{\mathrm{M}_{4,5}} \mathrm{d}\omega(\mu^{+}+\mu^{-}) = \frac{2}{3}\int_{\mathrm{M}_{4,5}} \mathrm{d}\omega(\mu^{+}+\mu^{-}+\mu^{0})$, $B = \int_{\mathrm{M}_5} \mathrm{d}\omega(\mu^{+}-\mu^{-})$, and $C = \int_{\mathrm{M}_4} \mathrm{d}\omega(\mu^{+}-\mu^{-})$ such that A is the integral over the XAS, and B and C are those over the XMCD across the Dy M_4 and M_5 edges as indicated for the integration range. The 2/3-factor in A takes into account the absorption of longitudinal polarization, which is not contained in our experimental XAS spectrum. However, because of the powder sample it can be set equal to the absorption of transverse polarization, justifying the simple calculation. $\langle T_z\rangle$ is the magnetic dipole operator. Since the 4f ions are very well described by L-S coupling and Hund's rules, and ligand fields have much weaker effects than in the 3d ions, $\langle T_z\rangle$ can be calculated analytically using eqs 8 and 9 in ref 15a, yielding a ratio of $\langle T_z\rangle / \langle S_z\rangle = -0.133$ for Dy^{III}.

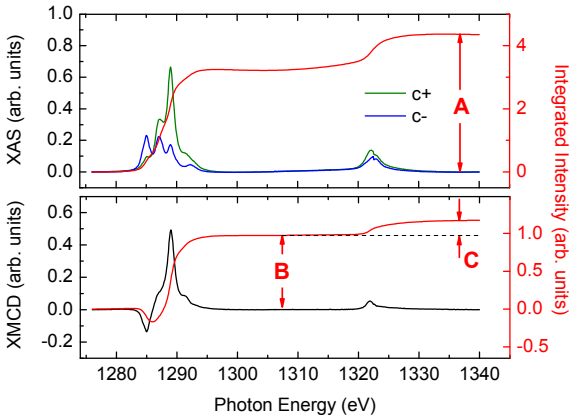

Fig. S3 (upper panel) X-ray absorption spectra on **1** at the Dy $M_{4,5}$ edges for the two indicated polarisations of the X-rays, recorded at 2 K and 6 T. The solid red line indicates the XAS integral. (lower panel) XMCD spectrum calculated from the data shown in the upper panel and XMCD integral.

To illustrate the sum-rules analysis, example X-ray absorption spectra on **1** along with the calculated XMCD spectrum are shown in Figure S3. The integral values *A*, *B* and *C* are indicated. The obtained spin and orbital as well as total magnetic moments for all measured spectra at different magnetic fields are summarized in Table S2. For high fields, "saturation" values between 5 and 6 μ_B are found for the total magnetic moment. In principle that would be in contradiction with the value of 10 μ_B expected from Hund's rules. However, the latter value would only be observed for an isotropic Dy^{III} ion in the absence of any ligand fields etc. The strong reduction compared to the free-ion value by a factor of ~2 originates from strong anisotropy. A calculation of the powder-averaged magnetic moment (using eqn S1) for a single Dy^{III} ion with only one Kramers doublet of $m_J = \pm 15/2$ yields a saturation magnetic moment of 5.0 μ_B. This is very close to the value observed by XMCD in our experiment.

Measurement	*B field* [T]	m_L [μ_B]	m_S [μ_B]	m_J [μ_B]
1	-1	-2.5(3)	-1.5(2)	-3.8(4)
2	+1	2.9(3)	1.6(2)	4.5(5)
3	-6	-3.5(4)	-2.1(2)	-5.6(6)
4	-6	-3.3(3)	-1.9(2)	-5.2(5)
5	+6	4.4(4)	1.6(2)	6.0(6)
6	+6	3.3(3)	1.9(2)	5.2(5)

Table S2. Values of the orbital and spin magnetic moments obtained for Dy using sum rules.

Ligand-field multiplet calculations

Multiplet calculations were carried out to simulate the X-ray absorption and X-ray magnetic circular dichroism for Dy^{III} and Cr^{III} using the TT-MULT program.[16] The results are shown in Figures 2b, 2d and 3b, 3d of the main text. For Dy the purely atomic calculation yields excellent agreement with the data. This is because the 4f levels are very localized, hence the X-ray absorption spectra at the $M_{4,5}$-edges of lanthanides are not very sensitive to ligand-field effects. Coulomb direct and exchange interaction are parameterised by Slater integrals, which were reduced to 60% of their atomic value for Dy^{III} and 80% for Cr^{III}. For Cr^{III} the calculation was done in D_{4h} symmetry with crystal field values of 10 Dq = 2.2 eV, Ds = –0.1 eV. Inclusion of ligand-to-metal charge transfer improves the agreement with the data. The charge transfer parameters used were $\Delta = 4$ eV, $T(A_1,B_1) = 2T(B_2,E)$ and $U_{dd} - U_{pd} = -1$ eV. Δ is defined as $E(d^{N+1}\underline{\mathbf{L}}) - E(d^N)$. In the final state of the X-ray

absorption process, the energy difference between the ionic and charge transfer configurations is given by $E(p^5d^{N+2}\underline{\mathbf{L}}) - E(p^5d^{N+1}) = \Delta + U_{dd} - U_{pd}$. T is the transfer integral between the metal d shell and the ligand p shell and is usually taken as being two times larger for the orbitals pointing along the bonding direction (A_1,B_1). At a field of –6 T, the expectation values $\langle S_z \rangle = -1.49$ and $\langle L_z \rangle = 0$ are found, in agreement with Cr^{III}. Simulations for both Cr^{III} and Dy^{III} were done considering a temperature of 2 K.

The above-mentioned parameters which were employed to simulate the Cr^{III} X-ray spectra can be compared to the values reported for $\{Cr^{III}F_2(py)_4\}^+$ in the literature.[17] From this, we obtain 10Dq = 2.3 eV, Ds = –0.125 eV and Dt = 0.0375 eV. These values are in excellent agreement with the parameters found from the multiplet calculations. Setting Dt = 0 in the calculations is justified because the observed X-ray absorption peaks are too broad (FWHM ~ 500 meV) to observe the associated energy splittings.

SQUID magnetometry

The temperature dependence of the in-phase component of the ac susceptibility of **1** is shown in Fig. S4 corroborating the SMM behaviour of **1**. Fig. S5 shows the magnetic-field dependence of the $\chi''(T)$ signal of **1** at a temperature of T = 1.8 K. At zero dc field the onset of a peak is visible but applying a small perturbing field further slows down magnetization relaxation.

The reduced magnetisation of **2** is shown in Fig. S6. The curves for different magnetic fields clearly do not superpose on each other, suggesting the presence of significant anisotropy and/or low-lying excited states. Fig. S7 shows the temperature dependence of χT of **2**. The room-temperature value of 15.5 cm^3 K mol^{-1} is consistent with the presence of a Dy^{III} ion with J = 15/2 (g_J = 4/3) and a Cr^{III} ion with S = 3/2 (g_S = 2) in the cluster, which would yield a theoretical value of 16.1 cm^3 K mol^{-1}. Between 300 K and 150 K the χT of **2** remains essentially constant, and below 50 K χT drops quickly. This may be due to the depopulation of ligand-field states of Dy^{III} and/or intracluster antiferromagnetic coupling. Ac magnetic measurements revealed no out-of-phase component ($\chi''(\nu_{ac})$ and $\chi''(T)$) above 1.8 K for **2** for all accessible static magnetic fields.

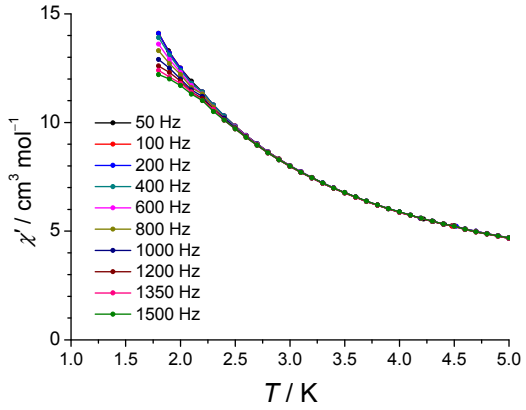

Fig. S4 In-phase component of the ac susceptibility of **1** as a function of temperature at selected frequencies of the oscillating magnetic field obtained with B_{dc} = 50 mT.

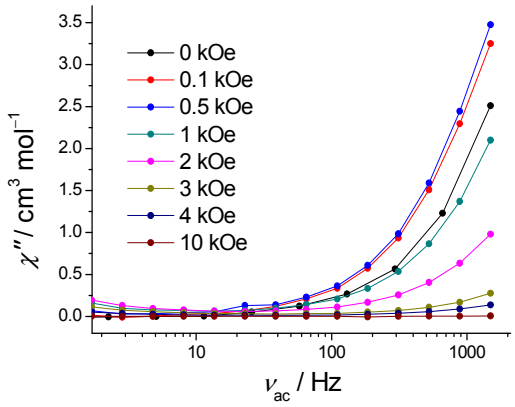

Fig. S5 Field dependence of the out-of-phase ac-susceptibility signal (χ'') for **1** measured at a temperature of 1.8 K.

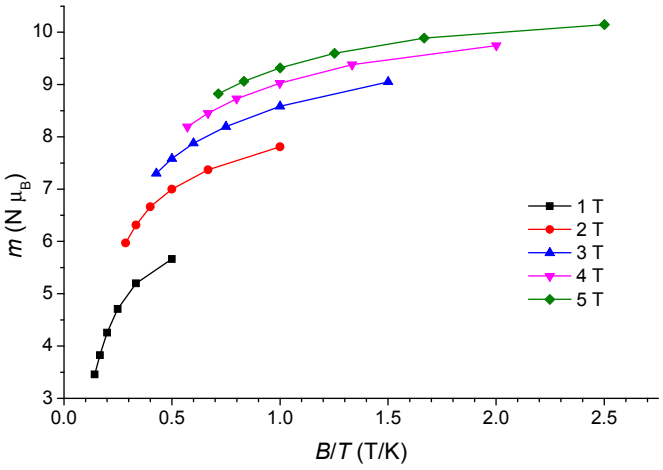

Fig. S6 Reduced magnetization of **2**. Solid lines are guides to the eye.

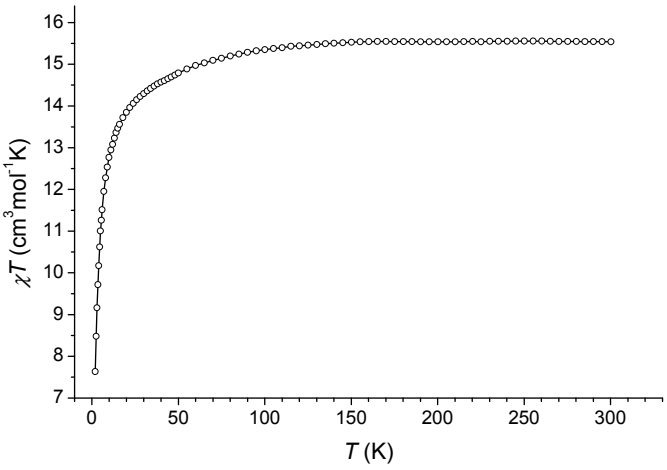

Fig. S7 Temperature dependence of the χT product of **2**. The solid line is a guide to the eye.

Inelastic neutron scattering

Information about the magnetic origin of INS features can be derived from their temperature and Q dependence. Upon increasing the temperature, magnetic excited energy levels become populated at the expense of ground-state-level population. This reduction of ground-state population leads to a decrease of INS transitions that correspond to excitation of the molecular magnet from the ground state to an excited state by a neutron, commonly referred to as "cold magnetic transition". In contrast, for harmonic vibrational modes the neutron energy loss response at a certain energy $E = \hbar\omega$ is proportional to the Bose factor[18] $1/[1 - \exp(-\frac{\hbar\omega}{k_B T})]$, which implies that the intensity can only stay constant or increase with increasing temperature. Furthermore, the Q-dependence contains relevant information, too. Here, Q is the absolute value of the momentum transfer, $Q = |\mathbf{Q}|$. At a constant energy E, for magnetic scattering the Q dependence is ruled by the magnetic form factors of the magnetic ions present in the cluster, and by their spatial coordinates.[19] Altogether, this leads to a decay of the scattering intensity with increasing Q. For incoherent scattering from vibrational modes the Q dependence is entirely different and the intensity is proportional to Q^2.[19]

In Figure 7a of the main text, features I and X were observed. Peak I appears at an energy of 3.4(2) cm^{-1} and possesses a full width at half maximum (FWHM) of 0.9 cm^{-1} which is close to that of the elastic peak of 0.8 cm^{-1}. The broad feature X is located at energy transfers from 9 to 16 cm^{-1}. Peak I shrinks with increasing temperature, while feature X is temperature independent. These features appear in the $S(Q,E)$ dependence shown in Figure S8, where they are indicated by black arrows. Whereas the scattering intensity $S(Q,E)$ at the energy of feature I decreases with Q, it exhibits opposite behaviour at the energy of the broad feature X. The latter is therefore proven to originate from a nonmagnetic excitation and can therefore be neglected in the further analysis of the magnetic properties of **1**. In contrast, feature I is inferred to be a cold magnetic transition.

The higher-resolution spectra shown in Fig. 7b of the main text reveal a three-fold splitting of feature I (energies 3.2(1), 3.7(1) and 4.3(1) cm^{-1}). The features Ia, Ib, Ic exhibit a linewidth of FWHM = 0.37 cm^{-1} which is equal to that of the elastic peak. The temperature dependence of features Ia-c suggests that they are all of magnetic origin. A closer look reveals that the temperature dependence of feature Ia is slightly weaker than that of Ib and Ic. Taking into account the small separation of 0.6 cm^{-1} between the peaks they can be attributed to transitions in the level scheme indicated in the inset of Fig. 7b. Further INS measurements at higher energy transfers do not reveal any other magnetic features up to an energy transfer of approximately 50 cm^{-1} as shown in Fig. S9.

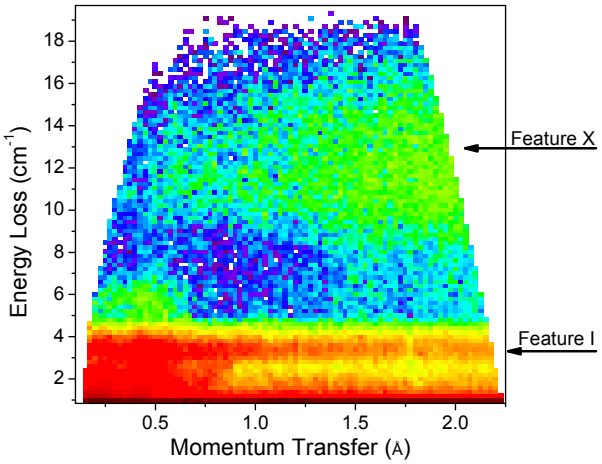

Fig. S8 Logarithmic plot of the $S(Q,E)$ dependence measured on **1** at a wavelength of λ = 4.8 Å and a temperature of 1.8 K. Red (violet) color represents strong (weak) intensity.

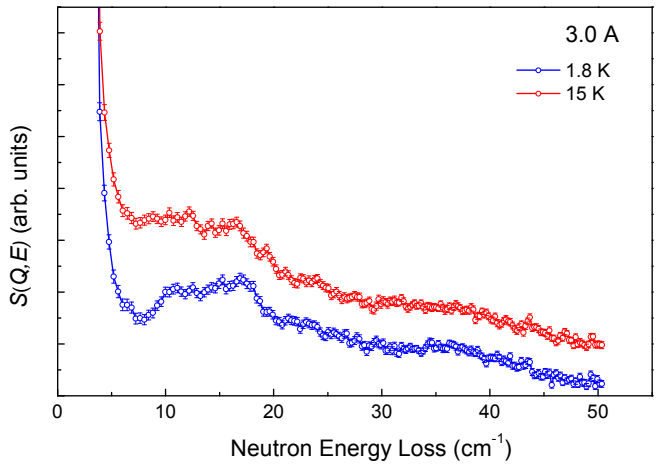

Fig. S9 INS spectra of **1** taken at a wavelength of λ=3 Å and temperatures as indicated in the plots. The intensity was summed for momentum transfers between 1.7 $Å^{-1}$ and 2.7 $Å^{-1}$. The curves were offset to improve visibility.

Muon-spin relaxation

The muon-spin relaxation data were analyzed using procedures similar as in ref. 20. Muon spin relaxation curves measured in zero magnetic field are presented in Figure S10. At low temperatures the asymmetry exhibits a dip within the first microsecond (inset of Figure S10), followed by a recovery and then relaxation at longer times. In contrast, at high temperature the asymmetry relaxes following an exponential curve. As discussed in ref. 20 the low-temperature relaxation curves are evidence that the internal magnetic field experienced by the implanted muons in **1** contains two contributions: a static component and a fluctuating component. Static (dynamic) fields are fields that fluctuate at a rate much slower (faster) than the muon lifetime of 2.2 μs. The static component is direct evidence of the slow relaxation of the magnetisation.

In the case of **1**, the asymmetry at all temperatures was found to fit best to a Lorentzian Kubo-Toyabe function multiplied by a square root exponential relaxation as represented by Equation 2 in ref. 20. The parameters λ and Δ extracted from the fits are shown in Figure S11. At high temperatures λ is small and $\Delta = 0$. Upon lowering the temperature λ increases strongly while Δ remains zero. At T^*~20 K, λ peaks and below this temperature Δ becomes non-zero. At lower temperatures λ further decreases and Δ saturates. The saturation values of 33 MHz correspond to a width in field of 40 mT. In analogy to ref. 20 the temperature-dependent relaxation time can be extracted as shown in Figure 6b in the main text. The relaxation time increases when the temperature is decreased but does not saturate down to 1.5 K, suggesting that the relaxation mechanism is thermally activated.

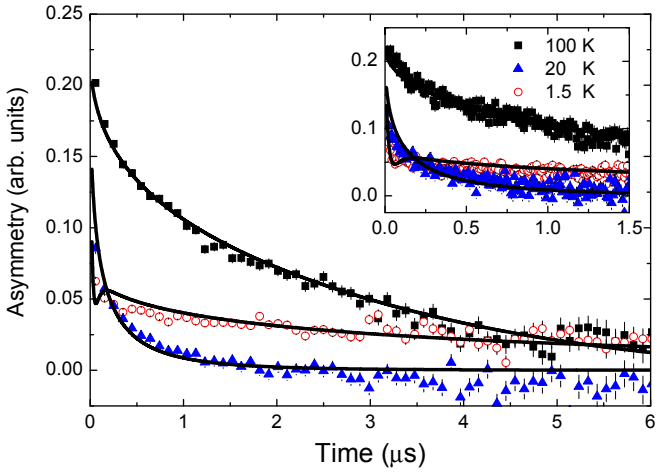

Fig. S10 Example muon-spin relaxation curves at three different temperatures. The inset shows a zoom into small timescales, where a clear dip in the relaxation can be seen at low temperatures, indicating the presence of static magnetic fields in the system.

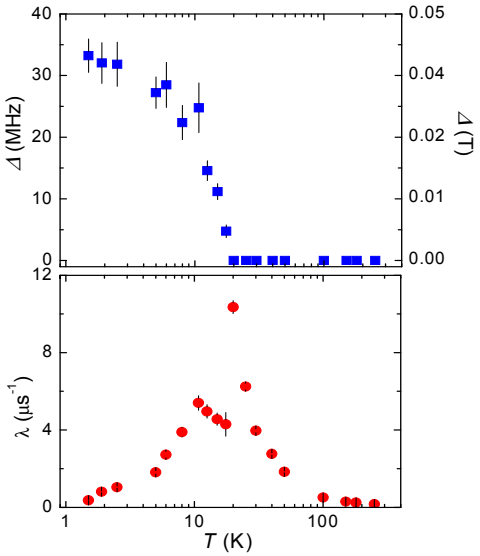

Fig. S11 λ (bottom) and Δ (top) obtained from fits to the relaxation curves as a function of temperature.

Spin-Hamiltonian models

A spin-Hamiltonian model is essential for extracting quantitive information from the data, such as the strength of the Dy-Cr exchange coupling. Our strategy was based on the following reasoning: On the one hand computationally efficient and simple models are needed. On the other hand it is desirable to reproduce a maximum of the experimental data. Furthermore, the number of free parameters typically decreases with decreasing complexity, mitigating problems of overparameterisation. Here we present the Hamiltonians following the order of decreasing complexity. The index i = 1,2,3 refers to the ion-site number within the trinuclear cluster, i.e. Dy(1)–Cr(2)–Dy(3). Details about the calculations are given on page 6 of the Experimental Section (ESI†). It is useful to start out with a spin Hamiltonian acting on the $J_1 = J_3 = 15/2$ ground multiplet of the Dy^{III} ions which we will refer to as *J-multiplet Hamiltonian*. The Cr spin takes the value $S_2 = 3/2$. The Hamiltonian is given by

$$\hat{H} = -j_{12}'\hat{\mathbf{J}}_1 \cdot \hat{\mathbf{S}}_2 - j_{23}'\hat{\mathbf{S}}_2 \cdot \hat{\mathbf{J}}_3 - j_{13}'\hat{\mathbf{J}}_1 \cdot \hat{\mathbf{J}}_3 + \sum_{i,k,q} B_{k,i}^q{}'\hat{O}_{k,i}^q \quad + \mu_B \sum_{i=1,3} g_i'\hat{\mathbf{J}}_i \cdot \mathbf{B} + \mu_B g_2'\hat{\mathbf{S}}_2 \cdot \mathbf{B} \qquad (S4)$$

The first two terms represent isotropic nearest-neighbour exchange couplings, and the third term is a much weaker coupling between the Dy^{III} ions. The fourth term describes the magnetic anisotropy induced by the ligand fields of the magnetic ions using Stevens operator notation. The last two terms represent the interaction with an applied magnetic field. Hamiltonian eqn S4 operates on the Hilbert space generated from the 16 states contained in each of the $J = 15/2$ multiplets of the Dy^{III} ions and another four states from the $S = 3/2$ multiplet of the Cr^{III} ion. Hence, the dimension of 1024 is fairly large. It is not only this dimension, which renders Hamiltonian eqn S4 rather impractical for

our simulations. More importantly, a vast number of magnetic anisotropy terms (for Dy: k = 2,4,6, q = –k, –k+1, ... +k) enter into the model because of the low symmetry of the two inequivalent Dy ligand fields. Hence, the very detailed model represented by Hamiltonian eqn S4 is strongly overparameterised, unless most of the free parameters would be determined by a dedicated series of additional measurements.

In order to significantly reduce the number of parameters we introduce a more practical Hamiltonian which operates in the restricted space of the ground state and the first-excited state Kramers doublets of each of the three ions. This *excited-state (encompassing) Hamiltonian* is given as eqn 1 of the main text. The terms are identical to those in the *J-multiplet* Hamiltonian but the number of anisotropy parameters is heavily reduced here. The maximally simplified Hamiltonian version is incorporated in the form of the spin-1/2 Hamiltonian given as eqn 2 of the main text.

We will now briefly discuss the interrelationship of the presented spin Hamiltonians eqns S4, 1 and 2. They describe the same magnetic system, which implies that there is a relation between spin-Hamiltonian parameters, e.g., j_{12}', j_{12} and $\mathbf{j}_{12,\mathrm{eff}}$. The same argument holds for anisotropy terms and **g**-matrices. Finding these relations is difficult in general, and in most cases the calculations can only be performed numerically. However, sometimes analytical relations can be derived with some approximations. Knowing such relations is useful. As an example, when the exchange coupling $\mathbf{j}_{12,\mathrm{eff}}$ in the spin-1/2 Hamiltonian has been determined which is rather simple because there are only a few free parameters, then j_{12} and j_{12}' can be readily calculated. This allows for consistent extensions of the basic spin-1/2 model to the more complex Hamiltonians.

Here, we focus on the relationship of g_i, $\mathbf{g}_{i,\mathrm{eff}}$, j_{ik}, and $\mathbf{j}_{ik,\mathrm{eff}}$ in eqs 1 and 2. A calculation using first-order quantum-mechanical perturbation theory treating the Zeeman term as the perturbation yields the following results, with $|m_{\mathrm{i,GS}}|$ the expectation value of the $\hat{J}_{i,z}$ operator for the ground state doublet of ion i = 1,3:

$$j_{12,\mathrm{eff},xy} = j_{12,\mathrm{eff},z} \cdot g_{1,\mathrm{eff},xy} / g_{1,\mathrm{eff},z} \qquad j_{23,\mathrm{eff},xy} = j_{23,\mathrm{eff},z} \cdot g_{3,\mathrm{eff},xy} / g_{3,\mathrm{eff},z}$$

$$j_{12,\mathrm{eff},z} = 2 j_{12} \, | m_{1,\mathrm{GS}} | \qquad j_{23,\mathrm{eff},z} = 2 j_{23} \, | m_{3,\mathrm{GS}} |$$

$$g_{1,\mathrm{eff},z} = 2 \, | m_{1,\mathrm{GS}} | \cdot g_J \qquad g_{3,\mathrm{eff},z} = 2 \, | m_{3,\mathrm{GS}} | \cdot g_J$$

(S5a-c)

If the ground-state Kramers doublets are eigenstates of the $\hat{J}_{i,z}$ operator (e.g. $m_{1,\mathrm{GS}} = \pm 15/2$), then the $j_{\mathrm{eff},xy}$ and $g_{\mathrm{eff},xy}$ terms will be zero. However, in non-uniaxial ligand fields the ground-state doublets can be admixtures (e.g. $|m_{1,GS}\rangle = \alpha|+15/2\rangle + \beta|-13/2\rangle$) and $j_{\mathrm{eff},xy}$ and $g_{\mathrm{eff},xy}$ can assume nonzero values.

Density-functional theory

Geometrical optimisation of the truncated model cluster as described on page 6 of the Experimental Section (ESI†) on the GGA level in scalar-relativistic approximation yields the Dy–F and F–Cr distances as 2.396 Å (exp. 2.321(2) Å) and 1.925 Å (exp. 1.903(2) Å). The non-bridging Cr–F distance is 1.862 Å (exp. in 2: 1.8440(15) Å and 1.8416(15) Å), the computed value is closer to that in the *trans*-$[CrF_2(py)_4]PF_6$ complex[21] (1.853(2) Å). The average Cr–N and Dy–O distances are 2.097 and 2.436 Å. The Cr–F–Dy bond-angle is 175.15° (exp. 176.49(13)°). Hence, the geometry is well reproduced.

References

[1] (a) J. Glerup, J. Josephsen, K. Michelsen, E. Pedersen and C. E. Schäffer, *Acta. Chem. Scand.*, 1970, **24**, 247, (b) M. F. Richardson, W. F. Wagner and D. E. J. Sands, *Inorg. Nucl. Chem.*, 1968, **30**, 1275.

[2] G. M. Sheldrick, *Acta Cryst.*, 2008, **A64**, 112.

[3] A. L. Spek, *PLATON, A Multipurpose Crystallographic Tool*, Utrecht University, Utrecht, The Netherlands, 2005.

[4] J. Krempasky, U. Flechsig, T. Korhonen, D. Zimoch, C. Quitmann and F. Nolting, *AIP Conf. Proc.*, 2010, **1234**, 705.

[5] S. L. Lee, S. H. Kilcoyne and R. Cywinski, *Muon Science;* SUSSP and Institute of Physics Publishing, 1998.

[6] (*a*) *LAMP, the Large Array Manipulation Program*. http://www.ill.fr/data_treat/lamp/lamp.html; (*b*) D. Richard, M. Ferrand and G. J. Kearley, *J. Neutron Research*, 1996, **4**, 33.

[7] (*a*) G. Kresse and J. Hafner, *Phys. Rev. B*, 1993, **47**, 558; (*b*) G. Kresse and J. Furthmüller, *Phys. Rev. B*, 1996, **54**, 11169; (*c*) P. E. Blöchl, *Phys. Rev. B*, 1994, **50**, 17953; (*d*) G. Kresse and J. Furthmüller, *Phys. Rev. B*, 1996, **54**, 11169.

[8] J. P. Perdew and J. Wang, *Phys. Rev. B*, 1992, **45**, 13244.

[9] M. Valiev, E. J. Bylaska, N. Govind, K. Kowalski, T. P. Straatsma, H. J. J. van Dam, D. Wang, J. Nieplocha, E. Apra, T. L. Windus and W. A. de Jong, *Comput. Phys. Commun.*, 2010, **181**, 1477.

[10] D. A. Pantazis, X.-Y. Chen, C. R. Landis and F. Neese, *J. Chem. Theory Comput.*, 2008, **4**, 908.

[11] Y. Zhao and D. Truhlar, *Theor. Chem. Acc.*, 2008, **120**, 215.

[12] (*a*) A. P. Ginsberg, *J. Am. Chem. Soc.*, 1980, **102**, 111; (*b*) L. Noodleman, *J. Chem. Phys.*, 1981, **74**, 5737; (*c*) L. Noodleman and E. R. Davidson, *Chem. Phys.*, 1986, **109**, 131.

[13] E. Ruiz, J. Cano, S. Alvarez and P. Alemany, *J. Comput. Chem*., 1999, **20**, 1391.

[14] V. I. Lebedev and D. N. Laikov, *Dokl. Math.*, 1999, **59**, 477.

[15] (a) P. Carra, B. T. Thole, M. Altarelli and X. Wang, *Phys. Rev. Lett.*, 1993, **70**, 694; (b) B. T. Thole, P. Carra, F. Sette and G. van der Laan, *Phys. Rev. Lett.*, 1992, **68**, 1943.

[16] (*a*) B. T. Thole, G. van der Laan, J. C. Fuggle, G. A. Sawatzky, R. C. Karnatak and J.-M. Esteva, *Phys. Rev. B*, 1985, **32**, 5107; (*b*) F. M. F. Groot, *Coord. Chem. Rev.*, 2005, **249**, 31.

[17] J. Glerup, O. Moensted and C. E. Schaeffer, *Inorg. Chem.*, 1976, **15**, 1399.

[18] G. Shirane, S. M. Shapiro and J. M. Tranquada, *Neutron Scattering with a Triple-Axis Spectrometer*, Cambridge University Press, Cambridge, England, 2002.

[19] (a) W. Marshall and S. W. Lovesey, *Theory of Thermal Neutron Scattering*, Oxford Clarendon Press, 1971; (b) Furrer, A., Güdel, H. U. *Phys. Rev. Lett.* **1977**, *39*, 657; (c) Waldmann, O. *Phys. Rev. B* **2003**, *68*, 174406.

[20] Z. Salman, S. R. Giblin, Y. Lan, A. K. Powell, R. Scheuermann, R. Tingle, and R. Sessoli, *Phys. Rev. B*, 2010, **82**, 174427.

[21] G. Fochi, J. Strähle and F. Gingl., *Inorg. Chem.*, 1991, **30**, 4669.